



**HAL**  
open science

# Garnet pyroxenites explain high electrical conductivity in the East African deep lithosphere

Thomas P. Ferrand, Emily Chin

► **To cite this version:**

Thomas P. Ferrand, Emily Chin. Garnet pyroxenites explain high electrical conductivity in the East African deep lithosphere. *Lithos*, 2023, 462-463, pp.107405. 10.1016/j.lithos.2023.107405. insu-04278415

**HAL Id: insu-04278415**

**<https://insu.hal.science/insu-04278415v1>**

Submitted on 8 Feb 2024

**HAL** is a multi-disciplinary open access archive for the deposit and dissemination of scientific research documents, whether they are published or not. The documents may come from teaching and research institutions in France or abroad, or from public or private research centers.

L'archive ouverte pluridisciplinaire **HAL**, est destinée au dépôt et à la diffusion de documents scientifiques de niveau recherche, publiés ou non, émanant des établissements d'enseignement et de recherche français ou étrangers, des laboratoires publics ou privés.

# Garnet pyroxenites explain high electrical conductivity in the East African deep lithosphere

Thomas P. Ferrand<sup>1,2</sup> & Emily J. Chin<sup>3</sup>

1: Institut für Geologische Wissenschaften, Freie Universität Berlin, Malteserstraße 74-100, Berlin 12249, Germany

2: Institut des Sciences de la Terre d'Orléans, CNRS UMR 7327, Université d'Orléans, France;

3: Geosciences Research Division, Scripps Institution of Oceanography, UC San Diego, La Jolla, USA.

Contact: [thomas.ferrand@fu-berlin.de](mailto:thomas.ferrand@fu-berlin.de)

---

## Abstract

In Tanzania, the deep lithospheric mantle (> 70 km depth) is characterized by significantly higher electrical conductivity within the cratonic root than in the Mozambique belt. Such contrasts are typically attributed to changes in volatiles and/or melt content, with changes in mineralogy deemed insufficient to impact conductivity. To test this assumption, electrical conductivity measurements were conducted at pressure-temperature conditions relevant to the Tanzanian lithosphere (1.5 and 3 GPa; from 400 to > 1500°C) on dunite (depleted) and pyroxenite (fertile) xenoliths from Engorora, Northern Tanzania. Once garnet becomes stable in the fertile mantle rock (> 60 km, 1.7 GPa), it nucleates at grain boundaries, forming the backbone of a conductive network. At 3 GPa, such garnet-rich networks increase conductivity by a factor of 100 regardless of temperature. Numerical models demonstrate that the observed low ( $< 10^{-2} \text{ Sm}^{-1}$ ) and high ( $> 10^{-1} \text{ Sm}^{-1}$ ) conductivity values can be explained by low and high degrees of garnet connectivity, respectively. Such high electrical conductivities in cratonic roots can be explained by the presence of connected garnet clusters or garnet pyroxenites, suggesting mantle fertilization. This new source for electromagnetic signal generation at appropriate pressures and temperatures must be factored in where interpreting magnetotelluric signals at relevant depths in the lithosphere.

---

**Keywords:** Craton, Mantle, Tanzania, Garnet pyroxenite, Lithosphere, Electrical conductivity.

---

### **Key Points:**

- Electrical conductivity measurements at high pressures and temperatures were conducted on dunite and pyroxenite xenoliths from Tanzania.
  - The high electrical conductivity is associated with networks of garnet pyroxenites, with natural H contents limited < 0.1 vol.%.
  - The high electrical conductivity in the root of the Tanzanian Craton would highlight current plume impingement.
-

## 34 Plain Language Summary

35 The deep root of the Tanzanian craton is characterized by high electrical conductivity. In this study, we  
36 reproduce this anomaly in the laboratory. We use powders of Tanzanian xenoliths, which are natural  
37 rocks similar to what is expected in the deep Tanzanian lithosphere. Two extremes of mantle  
38 composition are tested: dunite and pyroxenite, respectively typical of a depleted mantle (already  
39 produced melts) and fertile mantle (high chemical diversity). Experiments at high pressures and  
40 temperatures representative of the deep Tanzanian lithosphere reveal that the high electrical  
41 conductivity is generated by the establishment of a connected network of garnet pyroxenites. Minerals  
42 such as garnet and pyroxenes are known to conduct electricity much better than olivine – the major  
43 component of most mantle rocks – especially when they contain limited amounts of hydrogen. This  
44 "water" is incorporated in crystals and at their boundaries and promotes high-conductivity pathways. A  
45 significant increase in conductivity occurs once the pressure is high enough for garnet to become stable.  
46 These results suggest that the composition of the deep cratonic root in Tanzania is closer to a pyroxenite  
47 than a peridotite. This difference in composition compared to the average mantle is expected as an  
48 impact of the East African superplume.

---

## 49 1. Introduction

50 The structure and composition of the cratonic lithosphere has been debated for decades (e.g.  
51 Takahashi, 1990; Evans et al., 2011) but these deep regions of the Earth are only directly accessible via  
52 volcanically-derived xenoliths (e.g. Henjes-Kunst & Altherr, 1992; Vauchez et al., 2005; Doucet et al., 2014;  
53 Chin, 2018) and through indirect geophysical imaging (e.g. O'Donnell et al., 2013; Selway, 2015; Sarafian  
54 et al., 2018). The formation of cratons and their evolution through time are still under investigation (e.g.  
55 Liu et al., 2021), particularly their apparent longevity, although focus is also turning to processes of plume  
56 impingement that might eventually trigger craton disruption (Griffin & O'Reilly, 2007; Foley, 2008; Wang  
57 et al., 2015; Koptev et al., 2016). Magnetotellurics (MT) offers a powerful approach to understanding the  
58 structure of the lithosphere and upper mantle. For example, several studies report anomalously high  
59 conductivities in the lithospheric mantle, notably below the East African Rift (**Fig.1**; Selway, 2015; Sarafian  
60 et al., 2018). These anomalies are thought to provide evidence for the presence of volatiles and/or the  
61 occurrence of melting at depth (Selway, 2015).

62 A high-conductivity anomaly ( $> 10^{-2} \text{ Sm}^{-1}$ ) is observed below the Tanzanian Craton at depths  $> 70 \pm 10$   
63 km, while the conductivity of the neighboring Mozambique Belt at the same depth is much lower ( $< 10^{-3}$   
64  $\text{Sm}^{-1}$ ; Selway, 2015). The contrast between the cratonic root and the mobile belt is striking, and counter to

65 almost all observations in other similar tectonic settings (e.g. Evans et al., 2011; Sarafian, 2018). Selway et  
66 al. (2014) hypothesized that the high conductivity of the cratonic lithosphere is caused by the presence of  
67 water dissolved in olivine. However, this explanation contradicts models of cratonic root formation that  
68 consider predominantly depleted and dry roots. Furthermore, volatiles are known to lower mantle  
69 viscosity, enhancing the likelihood of mantle deformation (Hirth & Kohlstedt, 2003), which would not be  
70 consistent with craton stability. Most xenoliths have revealed that the non-metasomatized cratonic  
71 lithosphere is characterized by low bulk H content (~20-30 ppm H<sub>2</sub>O; Peslier et al., 2017), but this field is  
72 currently debated and methods evolve rapidly. Partly destroyed cratons such as the North China craton  
73 (NNC) can exhibit highly variable H contents, ranging from 10-100 ppm (northern NCC; Chin et al., 2020)  
74 up to 2900 ppm H<sub>2</sub>O (eastern NNC; Wang et al., 2022). The limited H contents observed in Kaapvaal  
75 xenoliths (South Africa) are consistent with observed low conductivities (Evans et al., 2011; Jones et al.,  
76 2012). In addition, pyroxenites from Hawaii, located over a mantle plume, are 4 times more hydrated than  
77 typical oceanic mantle (Bizimis & Peslier, 2015), which suggests that plume impingement could also  
78 increase the water content of cratonic roots. Yet, fertilization processes may depend on geological settings  
79 and would not necessarily require the action of a mantle plume (Griffin et al., 2009; O'Reilly & Griffin,  
80 2013).

81 To probe the origin of electrically-conductive cratonic environments, we experimentally reproduced  
82 the pressure-temperature conditions relevant to the deep Tanzanian lithosphere and performed electrical  
83 measurements on xenoliths from the area. The xenoliths originate from Engorora, Northern Tanzania  
84 (Chin, 2018). We used powders of a clinopyroxenite (ENG7) and a dunite (ENG8), two endmember  
85 lithologies in the area (Chin, 2018), hereafter referred to as fertile and depleted compositions, respectively  
86 (**Tables 1 and 2**).

## 87 **2. Material and methods**

### 88 **2.1. Starting Material: description, significance and representativity**

89 The Engorora xenoliths (Chin, 2018) consist of clinopyroxenites, wehrlites and dunites. In this study we  
90 used powders of a clinopyroxenite (ENG7) and a dunite (ENG8), which can be considered as two  
91 endmember mantle lithologies, hereafter referred to as fertile and depleted, respectively. Based on modal  
92 analysis and petrography from Chin (2018), ENG7 has 87% clinopyroxene, 11% orthopyroxene, 2% olivine,  
93 and trace amounts of chromite. Texturally, ENG7 has a poikilitic texture with clinopyroxene oikocrysts  
94 enclosing olivine and orthopyroxene chadacrysts. In general, grain size of the clinopyroxenite endmember  
95 xenoliths is variable and ranges from 1 mm to >5 mm. The clinopyroxenites do not show recrystallization

96 or other evidence of tectonic deformation. The dunite endmember xenoliths have a modal mineralogy of  
97 95% olivine, 4% clinopyroxene, and ~1% chromite. In contrast to the clinopyroxenites, the dunites have  
98 a very coarse-grained (~5 mm) and equigranular texture, and clinopyroxene, where present, is typically  
99 anhedral and often occurs interstitially between olivine grains.

100 Engorora, Chyulu (Southern Kenya) and the Lashaine area (10 km to the west from Engorora), are  
101 characterized by a large diversity of ultramafic xenoliths, including pyroxenites, lherzolites, harzburgites,  
102 wehrlites and/or dunites, the recorded depth of which depending on local specificities of volcanic systems  
103 (sampling depth). The magma ascent bringing xenoliths to the surface via volcanic eruptions involves  
104 percolation thresholds and local geological specificities, which lead to different sampling depths. For  
105 instance, the Engorora xenoliths contain spinel (Chin, 2018), while Chyulu exhibits mantle xenoliths  
106 containing connected garnet networks (Henjes-Kunst & Altherr, 1992), which does not mean that the  
107 Chyulu mantle would have more garnet on average. At depths >70 km, the lithospheric mantle contains  
108 garnet, but its amount and distribution can be highly variable (e.g. Lee & Rudnick, 1999).

109 The powders used in this study come from two endmembers of Engorora xenoliths. They present  
110 similar particle size distributions, with mean values of about 12 and 9  $\mu\text{m}$ , respectively (**Fig.S1**). Chemical  
111 compositions of ENG7, ENG8 and their host lava are provided in **Table 1**, along with compositions of their  
112 equivalent in Lashaine (Dawson et al., 1970) and of mantle rocks from a previous electrical conductivity  
113 study in China (Wang et al., 2008). The mineralogy and H contents of the Engorora xenoliths are provided  
114 in **Table 2**. Further details are listed in the **Supplementary Information (section 1)**, including carbon  
115 content (**Fig.S2**) and water content (**Fig.S3**) estimates.

## 116 **2.2. Experimental protocol**

117 All powders were stored in a desiccator to avoid water adsorption. Prior to experiments, the MgO parts  
118 of the assembly were fired to 1100°C during one hour and stored in a desiccator as well.

119 High-pressure, high-temperature experiments have been conducted using the 14/8 COMPRES electrical  
120 assembly (**Fig.2**) designed for electrical conductivity measurements in the multi-anvil (Pommier &  
121 Leinenweber, 2018). Each experiment was performed at a fixed pressure and the electrical conductivity  
122 was measured with increasing temperature, up to temperatures between 1400 and 1550°C depending on  
123 the experiment. The experimental conditions are summarized in **Table 3**, including available data on water  
124 and carbon contents, respectively estimated using SIMS and Raman measurements on the xenoliths from  
125 which the powders originate. An example of recovered quenched sample is presented in **Fig.3**.

126 Each experiment on peridotites and pyroxenites reported in this study has been performed with the  
127 same protocol (**Table S1**). First, pressure was increased from atmospheric pressure to the target pressure

128 over several hours, then temperature was increased from room temperature to  $\approx 400^\circ\text{C}$  for a short dwell  
129 to achieve electrical equilibrium. The temperature was then lowered to  $< 300^\circ\text{C}$  in order to start the  
130 experiment on an equilibrated system. Electrical measurements are then collected during heating until the  
131 sample is quenched at the highest T, except BB-238, for which a slow decrease of temperature was  
132 imposed after the peak temperature. Overall, the entire heating procedure until the target T of  $\approx 400^\circ\text{C}$  is  
133 reached and stable takes about 1h. During experiment BB-246, some instability in electrical measurements  
134 was noted upon heating ( $T < 800^\circ\text{C}$ ) after the dwell, and consequently the additional experiment BB-254  
135 was performed. Such instability is interpreted as due to high-pressure transformations at grain boundaries  
136 in light of kinetics considerations (as confirmed by microstructural observations, *section 3.2*).

137 To ensure reproducibility, experiment BB-246 has been reproduced with experiment BB-254 (**Table 3**).  
138 An additional experiment (BB-253) was performed on the pyroxenite powder up to  $750^\circ\text{C}$  only, i.e.  
139 quenched before any partial melting could occur, in order to check which microstructure was responsible  
140 for the drastic pressure-induced change in the conductivity values. No conductivity data were measured  
141 during this experiment. A summary of the experiments is provided in **Table 3**. The experimental conditions  
142 are illustrated on **Fig.4**, which also summarizes thermodynamic equilibrium of typical mantle peridotites  
143 and pyroxenites. Electrical conductivity and temperature measurements, with associated uncertainties,  
144 are described in the *Supplementary Information (section 2)*.

## 145 **3. Results**

### 146 **3.1. Microstructural analyses**

147 Retrieved assemblies were cut along the furnace and polished using sandpaper and diamond paste  
148 down to  $1\ \mu\text{m}$ . Microstructures (**Fig.5 to 9**) were imaged using a scanning electron microscope (SEM) at  
149 UCSD, Nanoengineering Facility. Mineral composition (**Table S2**) and element mapping (**Fig.S5** and **Fig.S6**)  
150 were acquired using energy dispersive X-ray spectroscopy (EDS).

151 In experiments performed at 3 GPa, microstructural observations reveal numerous garnet crystals,  
152 preferentially residing in the grain-boundary network of the pyroxenite samples (**Fig.5**); in the dunite  
153 samples sintered at 3 GPa, garnets are scarce and isolated (**Fig.8**). In contrast, for experiments on  
154 pyroxenites that reached 1.5 GPa only, microstructural observations do not reveal garnet growth but  
155 apparently stable Al-rich spinel (**Fig.9**). Some isolated grains of accessory phases are also observed in the  
156 samples (e.g. chromite, hibonite, metal alloys) but the spinel-garnet transition ( $\approx 1.8\ \text{GPa}$  in lherzolites) is  
157 the major metamorphic transformation in these conditions.

158 Counting pixels using *Adobe Photoshop* on **Fig.5b** (3 GPa;  $\leq 1400^\circ\text{C}$ ), the modal abundance of garnet is  
159 estimated to be a few percent, e.g.  $\sim 5$  vol.% for run BB-246. A similar analysis on **Fig.7a** (large garnet  
160 cluster around metal-rich inclusions) gives garnet fraction estimates of 7-8 vol.%, but the occurrence of  
161 local clusters cannot significantly increase the overall connectivity of the conductive garnet-rich network.

### 162 **3.2. Electrical conductivity**

163 At 1.5 GPa ( $\approx 50$  km depth) and over the investigated temperature range, the pyroxenite and dunite  
164 samples present similar conductivity values. These values would agree with a moderate bulk hydration  
165 ( $\sim 100$  ppm; Wang et al., 2006; Yang et al., 2011; Gardés et al., 2014), relative to typical cratonic mantle  
166 (Peslier et al. 2017). At 3 GPa ( $\approx 100$  km depth), dunite conductivity decreases by a factor ranging from 10  
167 to 100, depending on temperature (**Fig.10a**), whereas pyroxenite conductivity increases by a factor of  
168 about 10. The results at 3 GPa are in relatively good agreement with conductivities reported previously for  
169 dunite, lherzolite and pyroxenite containing minor H amounts ( $\sim 100$  ppm  $\text{H}_2\text{O}$ ), showing that pyroxenites  
170 are significantly more conductive (Wang et al., 2008), although less conductive than the Engorora  
171 pyroxenite xenolith (ENG7; **Fig.10a**). At high temperature ( $1300^\circ\text{C}$ ) the latter is as conductive as a silicate  
172 melt with moderate hydration ( $0.2 - 1 \text{ Sm}^{-1}$ ). According to SIMS measurements on cores of olivine and  
173 pyroxene crystals, the ENG7 and ENG8 samples contain at least moderate H amounts, but hydration alone  
174 cannot explain the contrast between the measured conductivity from 1.5 to 3 GPa (Dai et al., 2012; Gardés  
175 et al., 2014). The electrical transition between 1.5 and 3 GPa would therefore be due to garnet nucleation.

176 Because electrical conductivity provides information about the connectivity of conductive phases  
177 (Glover et al., 2000; Wang et al., 2013; Miller et al., 2015), the conductivity results (**Fig.10a**) are presented  
178 together with a range of connectivity models (**Fig.10b**) further described in **section 4**. These models  
179 assume diverse geometrical distributions of the conductive network within the samples, and are not scale  
180 dependent, which allows upscaling our results following representativity assumptions formulated and  
181 discussed in **sections 4** and **5**. In **Fig.10b**, the conductivity results at  $600^\circ\text{C}$  and  $800^\circ\text{C}$  are compared to the  
182 connectivity models, which allows us to estimate the expected amount (volume fraction) of the conductive  
183 network that is required in these models to explain the recorded electrical data.

### 184 **3.3. Garnet-rich networks as a plausible candidate to explain high electrical conductivity**

185 Microstructural observations illustrate that the electrical transition correlates with the nucleation of  
186 garnet, preferentially residing in the grain-boundary network of the pyroxenite samples (**Fig.5**). Electrical  
187 conductivity data suggest that the garnet pyroxenite network observed at 3 GPa in the pyroxenite is highly  
188 conductive ( $> 10^{-2} \text{ S.m}^{-1}$  at  $T > 750^\circ\text{C}$ , **Fig.10a**). Iron increases garnet conductivity (Dai et al., 2012), due to  
189 the decrease of the average distance between  $\text{Fe}^{2+}$  and  $\text{Fe}^{3+}$  (Romano et al., 2006). It should be noted that

190 similar values are obtained if the garnet composition is  $\sim\text{Py}_{73}\text{-Alm}_{14}\text{-Grs}_{13}$  ( $\approx 5.6$  wt.% Fe; Dai et al., 2012)  
191 and  $\text{Py}_{85}\text{-Alm}_{15}$  ( $\approx 6$  wt.% Fe; Romano et al., 2006). Despite the small size of the nucleated garnet crystals  
192 in the recovered samples, an approximate formula of  $\sim\text{Py}_{51}\text{-Alm}_{18}\text{-Grs}_{31}$  ( $\approx 6.9$  wt.% Fe) is obtained using  
193 EDS measurements (**Table S2**; **Fig.S5** and **S6**). Since garnet is surrounded by Fe-poor, Ca-rich  
194 clinopyroxenes, the almandine fraction (Alm) represents a compositional lower bound (i.e. the garnet iron  
195 content is  $\geq 6.9$  wt.%). Nonetheless, the conductivity of dry  $\text{Py}_{20}\text{-Alm}_{76}\text{-Grs}_4$  ( $\approx 26.7$  wt.% Fe) garnet does  
196 not exceed  $10^{-3}$  S.m<sup>-1</sup> at 850°C (Dai et al, 2012), which is 100 times lower than the measured bulk  
197 conductivity value (**Fig.10b**). Therefore, the high conductivities of the pyroxenite samples cannot be solely  
198 attributed to the iron content of the garnet. Including minor water within garnets and pyroxenes could,  
199 however, reproduce the observations. The conceptualization and extrapolation to nature is provided in  
200 **section 4** and **section 5**, respectively.

201 The presence of garnet, expected according to both thermodynamics, is evidenced by microstructural  
202 observations (**section 3.2**) of samples retrieved after experiments at 3 GPa (**Fig.5** to **Fig.S6**). In various  
203 natural lithologies, garnet is reported as preferentially distributed in layers or channels (**section 4.1**); in  
204 our experiments, garnet, which represents some vol.% at 3 GPa (up to  $\sim 5$  vol.% in **Fig.5b**), is preferentially  
205 distributed along grain boundaries, where reactive phases are in contact (**section 4.2**) and where diffusivity  
206 is enhanced (Fisher, 1951). Garnet networks have been observed in xenoliths (Henjes-Kunst & Altherr,  
207 1992) in the same region (Chyulu, Southern Kenya; **Fig.S7a**, located in **Fig.1**), which can be seen as an  
208 analogue of the experimental garnet-rich networks. Thus, the experiments at 3 GPa would be  
209 representative of larger-scale natural features and we argue that their bulk electrical response is relevant  
210 to interpret the deep conductive anomaly.

211 The electrical data highlight a transition in the electrical response of the pyroxenite and dunite samples  
212 between 1.5 and 3 GPa, respectively characterized by an increase and a decrease in conductivity. Both  
213 xenoliths contain minor carbon impurities located at grain boundaries (**Fig.S2**), consistently with the  
214 literature (Watson, 1986; Pearson et al., 1994), which would be consistent with the CO<sub>2</sub>-rich magmatism  
215 observed in the area and oxygen fugacity considerations (**Discussion**). Solid carbon (either graphite or  
216 amorphous carbon) is known to be highly conductive ( $\sim 10^5$  S.m<sup>-1</sup>; Duba & Shankland, 1982) and thus  
217 significantly enhance conductivity when connected ( $\geq 1$  wt.%; Wang et al., 2013). However, a recent study  
218 revealed that carbon grain-boundary films are not stable at upper-mantle pressures (reductive conditions)  
219 and that carbon is thus unlikely to explain the high-conductivity anomalies revealed by MT surveys in the  
220 upper mantle (Zhang & Yoshino, 2017). In addition, there is no reason for carbon to become more



221 conductive/connected with increasing pressure. Consequently, the presence of carbon alone is insufficient  
222 to explain the data.

223 In the experiments reported in this study, the increase of conductivity is limited to pyroxenites because  
224 in dunites (i.e. > 90% olivine) the connectivity of the (rare) conductive minerals is close to zero. However,  
225 in nature, mantle rocks such as foliated lherzolites could well be as conductive as garnet pyroxenites, as  
226 long a relatively dense conductive network exists and is connected (see conceptualization in **section 4** and  
227 discussion in **section 5**).

## 228 **4. Conceptualization and forward modelling**

### 229 **4.1. Widespread hydrous garnets and pyroxenes in the mantle**

230 Although water is widely reported to be incorporated into pyroxenes (~ 100 ppm), garnet can also  
231 accommodate a significant H amount in its crystal lattice (~ 1000 ppm H<sub>2</sub>O; Aines & Rossman, 1984;  
232 Maldener et al., 2003). A review of limited (≈ 500 ppm H<sub>2</sub>O) to high (≈ 2500 ppm H<sub>2</sub>O) amounts of hydrogen  
233 in natural garnets is provided by Ferrand (2020). The garnet identified in this study (3 GPa) has the  
234 approximate formula ~Py<sub>51</sub>-Alm<sub>18</sub>-Grs<sub>31</sub>, which is, considering the explanations hereabove, ideal for  
235 hydrogarnet stability. The high affinity of garnet and pyroxene crystals for hydrous defects (e.g.  
236 hydrogarnet) should lead high H contents in the microcrystalline grain-boundary paragenesis. Consistently  
237 with recent reviews (e.g. Peslier et al., 2017) and with the high affinity of garnet for hydrous defects  
238 compared to other mantle minerals, we consider water contents of the garnet pyroxenite networks  
239 between 50 and 500 ppm.

240 Electrically, water in garnet significantly increases conductivity; for instance, hydrous pyrope (with 465  
241 ppm H<sub>2</sub>O) is 100 times more conductive at 750°C than its anhydrous counterpart (**Fig.10b**; Dai et al., 2012).  
242 The only studies that have investigated the electrical conductivity of hydrous garnets used a pyrope from  
243 Garnet Ridge, Arizona, USA, of composition ~Py<sub>73</sub>-Alm<sub>14</sub>-Grs<sub>13</sub> (Dai & Karato, 2009; Dai et al., 2012), with  
244 H contents of 465, 160 and 46 ppm H<sub>2</sub>O. A value of 465 ppm is assumed in **Fig.10** and **Fig.11**. The impact  
245 of H content on the simulations is addressed in **Fig.12**.

246 In **section 5**, electrical anomalies in the deep Tanzanian lithosphere are reappraised in light of our  
247 experimental results (**Fig.13**). Two endmember scenarios are considered, depending on the amount and  
248 connectivity of garnets: the deep Tanzanian lithosphere is composed of either (1) fertile mantle rocks with  
249 garnet-rich networks or (2) depleted mantle rocks without garnet-rich networks.

### 250 **4.2. Garnet pyroxenite formation and connectivity**

251 Reaction kinetics is key in the development of metamorphic microtextures (Ridley & Thompson, 1986).  
252 Studies have reported garnet nucleation and growth at low temperatures (Lanari & Engi, 2017 and  
253 references therein). Notably, garnet crystals (5 mm average diameter) are reported in the southern  
254 Omineca belt of the Canadian Cordillera, which underwent Barrovian metamorphism peaking at middle  
255 amphibolite facies during the Early Cretaceous. Garnet porphyroblasts grew along a P-T path from 500°C  
256 at 0.5 GPa to 570°C at 0.7 GPa. For comparison, in experiment BB-253 ( $\leq 750^\circ\text{C}$ , 3 GPa), submicrometric  
257 garnet crystals grew at grain boundaries in less than 2 hours at  $T > 400^\circ\text{C}$ .

258 Most experimental petrology experiments focus on high temperatures for two reasons: 1) in nature,  
259 garnet nucleation and growth at  $T < 500^\circ\text{C}$  in ultramafic rocks is rather unrealistic, and 2) high  
260 temperatures are required for grain growth to occur fast enough during an experiment in order to perform  
261 single-grain analyses with various techniques.

262 Polymorphic transformations such as the quartz-coesite transition can easily occur at low temperatures  
263 because it requires no or limited atomic diffusion. Contrastingly, the “spinel-garnet transition”, i.e.  
264 transition from a spinel lherzolite/pyroxenite to a garnet lherzolite/pyroxenite, is a metamorphic reaction  
265 involving the reorganization of several phases within a paragenesis, i.e. at the scale of several grains (e.g.  
266 Lanari & Engi, 2017, and references therein). For such metamorphic reaction, the thermodynamics is highly  
267 impacted by kinetics, which allows at low temperatures the preservation of metastable HP-HT rocks  
268 eventually exposed to the surface after the erosion of internal mountain belts. Especially, any reaction  
269 that involves garnet formation involves  $\text{Al}^{3+}$  diffusion, which is slow at  $800^\circ\text{C}$ .

270 Another parameter controlling reaction kinetics is thermodynamic overstepping, which is a driving  
271 force that is necessary for porphyroblast nucleation and growth (Spear, 2017). The growth of nanometric  
272 garnets likely initiated during the initial sintering process. At such low temperatures, the reaction occurred  
273 only where the reactive minerals are close to each other, i.e. at grain boundaries. Although  $\text{Al}^{3+}$   
274 intracrystalline diffusion is slow, we consider that the original garnet-rich network in the samples at  
275 temperatures between 400 and  $800^\circ\text{C}$  is the result of the small grain size and favoured contacts between  
276 the reactive minerals during initial heating and powder compaction. Considering a Stefan’s interface model  
277 for garnet growth, the growth of crystals at  $700^\circ\text{C}$  up to a radius of 10 or 100 nm is feasible in a few minutes  
278 and a few hours, respectively (Spear, 2017; Mg-poor system). Some garnet grains are larger (up to  $\approx 1 \mu\text{m}$   
279 in radius at  $750^\circ\text{C}$ ; **Fig.S6**), which can be due to both the large pressure overstep ( $\Delta P > 1 \text{ GPa}$ ; **Fig.4**) and  
280 larger diffusivity in Mg-rich systems compared to Mg-poor systems.

281 The garnet-rich network developing at grain boundaries is an example of local mineral assemblage due  
282 to slow metamorphic reactions within the intergranular system, referred to as grain-boundary equilibrium

283 (Lanari & Engi, 2017). Even though most garnet grains are much smaller at 750°C (BB-253; **Fig.6** and **S6**)  
284 than at 1400°C (BB-246; **Fig.7** and **Fig.S5**), the garnet network is already well developed, which explains  
285 the high conductivity even at low temperatures (500-750°C; **Fig.10**). Garnet connectivity was reported in  
286 various natural rocks (e.g. Henjes-Kunst & Altherr, 1992; John et al., 2004; Evans et al., 2011; Vrijmoed et  
287 al., 2013; Lanari & Engi, 2017). The connectivity of garnet networks or garnet pyroxenites is documented  
288 by several studies in different geological contexts (e.g. Henjes-Kunst & Altherr, 1992; Vrijmoed et al.,  
289 2013).

### 290 **4.3. Network connectivity and electrical conductivity**

291 The interconnection of conductive phases and the topology of the conductive network control the bulk  
292 electrical conductivity of a multiphase system (e.g. Glover et al., 2000; Wang et al., 2013; Miller et al.,  
293 2015). In the system considered in this study, we have to consider two networks which themselves  
294 combine to form the bulk conductivity. The first of these networks consists of the various minerals that  
295 compose the host rock. The second is the material within the grain boundaries that contains a complex  
296 distribution of phases, which we refer to as the intergranular system.

297 The starting material that forms the host is a relatively homogeneous distribution of submicrometric  
298 to plurimicrometric grains of olivine, pyroxenes and accessory minerals. We used a random-distribution  
299 model to compute the bulk conductivity of the host rock based on the documented conductivity data of  
300 each phase. Although dealing with different time and space scales, the conceptualization in the present  
301 study follows the same logic as presented by Ferrand (2020). Considering a harmonic mean with arbitrary  
302 shaped and oriented volumes of conductivity  $\sigma_i$  and fraction  $X_i$ , a random model can be used to calculate  
303 the bulk conductivity  $\sigma^*$  as follows:

$$304 \quad \sigma^* = \prod_{i=1}^N \sigma_i^{X_i}$$

305 Conductive grain-boundary impurities can significantly impact the bulk conductivity, and their influence  
306 depends on their amount and nature (Watson et al., 2010). Consequently, the conductivity within the  
307 grain-boundary network is less straightforward, as it consists of garnets, carbon and other phases  
308 distributed in a complex manner. However, when considering the effects of minor carbon impurities  
309 (**Fig.S2**), likely graphitic in the cratonic root (**section 5.2**), and given that there is no reason for carbon to  
310 be anisotropically distributed in the powder, the random model can also be used to estimate the  
311 conductivity of the carbon-bearing garnet-rich network. An alternative estimate would be to consider  
312 carbon impurities as electrical shorts between the garnet grains. The random model provides a more  
313 conservative estimate and is chosen for bulk calculations.

314 It should be noted that, considering that the carbon impurities are localized at grain boundaries, the  
315 carbon content of the grain-boundary conductive network is necessarily significantly larger than the bulk  
316 carbon fraction. While the bulk graphite content is estimated to be  $\sim 0.1$  wt.%, we expect, considering the  
317 intergranular system equal to 3-10% of the total volume, that the average graphite content of the grain  
318 boundaries is  $< 10$ -30 vol.%. In **Fig.10** and **Fig.11**, a garnet/graphite ratio of 80:20 is assumed. Because the  
319 uncertainty about the carbon amount in both the experimental conductive network and its natural  
320 equivalent, **Fig.12** also presents simulations for ratios 70:30 and 90:10. Electrical conductivity values for  
321 given fractions of garnet and carbon are provided in **Table S3**. In the deep root of the craton, the expected  
322 form of carbon is thermodynamically stable one in mantle rocks equilibrated in reductive conditions, i.e.  
323 graphite, which electrical conductivity is not much higher than amorphous/disorganized carbon (Duba &  
324 Shankland, 1982), in comparison to silicates.

325 Several models exist to predict the bulk conductivity of rocks as a function of a conductive interstitial  
326 phase, typically partial melt or saline fluid (e.g. Glover et al., 2000 and references therein). Connectivity  
327 problems can be solved using the percolation theory (Gueguen & Dienes, 1989). The connectivity threshold  
328 depends on the geometry of the conductive network (e.g. Miller et al., 2015). This geometry is analogous  
329 to the melt-grain networks analyzed by Zhu et al. (2011) and Miller et al. (2015), except that instead of a  
330 homogenous melt phase (with a single conductivity value), we have a multi-phase network between grains  
331 that includes garnet and carbon as discussed above. Complementary carbon-free models have been  
332 published in a previous study to reproduce the conductivity of garnet pyroxenite channels (Ferrand, 2020).

333 We have compared the geometry-based models to a modified Archie's law accounting for the  
334 conductivity of both the conductive network and the silicate grains (Glover et al. 2000) (**Table S3**). Miller  
335 et al., (2015) found that such modified Archie's law is relevant to interpret bulk conductivity values as a  
336 function of melt fraction. Using microtomography in partially molten rocks (Zhu et al., 2011; Miller et al.,  
337 2015), it was observed that the connectivity threshold strongly differs between 2-D and 3-D systems (e.g.  
338 Clerc et al., 1979), which implies that the expected connectivity level in the samples is necessarily higher  
339 than what can be observed with SEM imaging (**Fig.5 to 8**).

340 We have used a variety of multi-phase conductivity models shown in **Table S4** in order to cross-check  
341 the bulk conductivities measured in the laboratory. Several volume fractions were tested and preferred  
342 models correspond to the ones that reproduce the observations. As illustrated in **Fig.11**, considering a  
343 moderate garnet hydration and the presence of a minor amount of graphite, the conductive grain-  
344 boundary network is expected to represent only 1-3 vol.%. Regarding the geometry of the garnet-rich  
345 network, it appears that either the Hashin-Shtrikman upper bound, the wetted thin films or the modified

346 brick-layer models provide simulations that fit the data (**Fig.11**). Considering the uncertainty regarding  
347 both the carbon fraction and the exact H content of garnet, additional simulations show that the  
348 conductivity values obtained during the experiments at 3 GPa can be explained by the nucleation of  
349 nanometric garnet crystals at grain boundaries. We consider the conductive network described above as  
350 an experimental equivalent of larger-scale natural garnet-rich networks, such as garnet pyroxenite  
351 layers/clusters that are expected in the metasomatized root of the Tanzanian craton (**section 5.1; Fig.S7**).

## 352 **5. Extrapolation to nature and discussion**

### 353 **5.1. Significance of the experimental results for the deep cratonic root.**

354 Electrical models considering various connectivity modes (**Fig.10, Fig.11, Fig.12**) suggest that the bulk  
355 conductivity of pyroxenite (e.g. BB-246; **Fig.5b**) is best reproduced by the presence of a garnet-rich grain-  
356 boundary network containing scarce carbon impurities. As a consequence, we suggest that the  
357 combination of a moderate H amount, the presence of iron in garnet, and the preferential distribution of  
358 garnet grains and carbon impurities at the grain boundaries best explains the high electrical conductivity  
359 of the pyroxenite samples at 3 GPa. This garnet-rich grain-boundary network can be seen as a laboratory-  
360 scale experimental analogue of larger-scale natural garnet-rich features (Henjes-Kunst & Altherr, 1992;  
361 Vrijmoed et al., 2013).

362 Garnet is ubiquitous in the deep cratonic lithosphere (> 2 GPa, i.e. > 60 km depth), but the conductive  
363 anomaly is located deeper than the top of the garnet stability field (> 2.7 GPa, i.e. > 80 km depth; **Fig.4** and  
364 **13a**). Furthermore, if the transition to the garnet stability field was solely the cause of the conductive  
365 anomaly, such a transition should be a ubiquitous feature within cratons globally, yet that is not the case.  
366 In Tanzania, the conductive anomaly corresponds to the deepest part of the cratonic lithosphere. The  
367 widespread presence of garnet at these depths is consistent with previous studies that argue for increased  
368 fertility with depth, associated with recent plume impingement, from which the Fe-rich dunites of the area  
369 would also originate (Lee & Rudnick, 1999). As a consequence, we propose that the garnet-rich networks  
370 originate from plume-induced metasomatism (**section 5.4**).

371 As illustrated in **Fig.13**, the experimental results on the pyroxenite and dunite at 3 GPa (**Fig.10b**)  
372 reproduce the field conductivity values reported by Selway (2015) for the deep lithosphere of the craton  
373 and the neighboring belt, respectively. We propose that the electrically conductive anomaly below the  
374 craton is caused by the presence of garnet-rich network in a similar manner to the networks observed in  
375 the pyroxenite samples (**Fig.13e**). The numerical models of electrical conductivity are scale-independent  
376 and can apply to the thin grain-boundary networks in experimental samples and to larger garnetite or

377 garnet pyroxenite layers in nature. Scattered graphitic impurities, commonly introduced by plume  
378 metasomatism, may contribute to the electrical network. As previously noted (Selway, 2015), partial  
379 melting is not a plausible candidate to explain the field electrical observations, as both high shear-wave  
380 seismic velocities (O'Donnell et al., 2013) and a cool geotherm (Vauchez et al., 2005) characterize this  
381 craton. Instead, it was suggested that the conductive anomaly could be due to a H content significantly  
382 higher in the cratonic mantle than in the highly deformed Mozambique Belt (Selway, 2015). This  
383 contradicts the long-term stability of the craton and rheological studies highlighting that deformation is  
384 enhanced by the presence of water (Hirth & Kohlstedt, 2003), though differences in grain size could  
385 counter the water-induced weakening, allowing the cratonic root to remain stable (Selway, 2015).

386 Our results also reconcile the apparent discrepancy between MT (high conductivity) and seismic  
387 observations (fast velocities) within deep cratonic roots at  $70 \pm 10$  km depth (O'Donnell et al., 2013). The  
388 volume fraction of garnets required for the electrical model are not so substantial that a significant impact  
389 on bulk seismic velocity should be expected. It should be noted, however, that an enigmatic seismic  
390 discontinuity was evidenced beneath North America around these depths (Hales, 1969). Both the results  
391 and simulations (**Fig.10 to 12**) recall that the connectivity of conductive minerals is the main parameter  
392 controlling bulk electrical conductivity, rather than their actual volume fraction. Hence, the garnet fraction  
393 needed to explain the electrical structure is sufficiently small that a commensurate change in seismic  
394 velocities is not expected (James et al., 2003). Although the distribution of garnet-rich networks within the  
395 deep Tanzanian lithosphere is unknown, occurrences of garnet interconnected over long distances are  
396 observed in nature. In our samples, the conductive network contains minor amounts of carbon. The root  
397 of the craton is reported as the source of carbon enrichment (Muirhead et al., 2020). Garnet networks,  
398 reported both in xenoliths (**Fig.S7**; Henjes-Kunst & Altherr, 1992) and outcrops (Vrijmoed et al., 2013), can  
399 be caused by mantle fertilization.

400 Although conductive lithospheric mantle is not ubiquitous in cratons, there are examples of elevated  
401 lithospheric conductivity, including the rifted Yilgarn craton, Australia (Wang et al., 2014) and the Dharwar  
402 craton near the Deccan traps, India (Patro & Sarma, 2009). The North China craton is thought to have been  
403 disrupted by plume impingement (Wang et al., 2015) and has a signature that reflects thinner lithosphere  
404 after delamination (Ye et al., 2018). Metasomatism due to plume impingement has been suggested as a  
405 potential cause of the destruction of cratons (Foley, 2008; Wang et al., 2015; Celli et al., 2020). Elevated  
406 conductivities suggest extensive metasomatism by the African superplume, a model supported by  
407 numerical modelling for the East African rift system in the area (e.g. Koptev et al., 2016). Thus, the MT

408 model of Tanzania (Selway et al., 2015) could present an image of lithosphere primed to break away. Root  
409 delamination would eventually erase the conductive anomaly.

## 410 **5.2. Type and amount of carbon present & oxygen fugacity**

411 Northern Tanzania is volcanically active – a prime example is Mt. Kilimanjaro – and the lithospheric  
412 mantle of the region is known to be CO<sub>2</sub>-rich, as revealed by various xenoliths containing either carbonates  
413 (e.g. Lee & Rudnick, 1999) or carbonatite metasomatism (Rudnick et al., 1993). Xenoliths of the Lashaine  
414 area contain about 3 wt.% of H<sub>2</sub>O and 1.4 wt.% of CO<sub>2</sub> (Dawson et al., 1970), which suggests that the  
415 lithospheric mantle contains 10-100 ppm of CO<sub>2</sub> on average. This is further confirmed by a recent work in  
416 the studied area (Halldórsson et al., 2022), reporting high CO<sub>2</sub> contents between 0.6 to 1.7x10<sup>-6</sup> cm<sup>3</sup>/g in  
417 pyroxenite xenoliths. At high pressure (> 1 GPa) in the mantle, reductive conditions should favor graphitic  
418 carbon impurities at grain boundaries, which can be easily identified and speciated using Raman  
419 spectrometry (e.g. Pearson et al., 1994). Yet, Raman spectrometry reveals limited crystallinity (**Fig.S2**), as  
420 explained in details in the literature (e.g. Deldicque et al., 2023). The relatively cold geotherm of the craton  
421 induces kinetics issues within the studied xenoliths that maintain the carbon in a less mature state (**Fig.S2**),  
422 expected almost as conductive (Duba & Shankland, 1982; Watson, 1986); in contrast, the deep root should  
423 host graphitic carbon at grain boundaries due at intermediate temperatures.

424 The preservation of the rhenium furnace, along with the stability of minor grains of Th-Ta-Ni alloy and  
425 the presence of titanium phosphide (**Fig.S5** and supplementary text) indicate a reducing environment, as  
426 expected in the cratonic mantle at 3 GPa (log *f*O<sub>2</sub> = -2; ΔFMQ; Frost & McCammon, 2008). In such reduced  
427 conditions at elevated temperatures, carbon is more likely in the form of graphite that immobilizes at grain  
428 boundaries (Watson, 1986). This confirms that the studied xenoliths originate from relatively shallow  
429 depths, consistently with the absence of garnet in the starting material. In contrast, higher temperatures  
430 in the root of the craton would favor graphitization of such organic matter. It should be noted that the  
431 term ‘graphitic carbon’ is often used as a general description of carbon in conductivity studies, because  
432 carbon crystallinity is a minor parameter compared to its connectivity.

433 Both the nature and repartition of the carbon impurities should be considered to evaluate the impact  
434 of carbon on electrical conductivity (Wang et al., 2013). A previous study determined a percolation  
435 threshold of graphite GB impurities of ~ 1 wt.% (Wang et al., 2013), while lower graphite contents (~ 0.1  
436 wt.%) are associated with relatively low bulk conductivities (Watson et al., 2010). In the model, we assume  
437 the carbon content ~ 0.1 wt.% based on Raman spectrometry (**Fig.S2**) and consistently with regional  
438 constraints (Dawson et al., 1970; Chin, 2018; **Table 1**), and evidence the nucleation of nano- to microgarnet  
439 at grain boundaries, likely involving carbon impurities in the conductive network (**Fig.11, Fig.12**).

440 In addition, carbon solubility in olivine is relatively low compared to pyroxenes and garnet, but  
441 increases with pressure (Keppler et al., 2003). As ENG8 consists of 95% olivine, it is possible that the  
442 observed drop in conductivity with increasing pressure is due to the effect of pressure as well as enhanced  
443 carbon solubility.

### 444 **5.3. Remarks on the electromagnetic profile**

445 Although the focus of the present study is the root of the Tanzanian craton, the MT profile (Selway  
446 (2015) shown in **Fig.13** presents other high-conductivity anomalies, localized at shallow depths ( $\leq 35$  km  
447 depth;  $\approx 1.1$  GPa) in magmatic areas. These anomalies require other explanations, such as melt networks  
448 or hydrothermal fields. Such melt networks may correspond to the mature rift system of the Central Vallee,  
449 Ethiopia, where near-surface high conductivity ( $\sim 1$  S.m<sup>-1</sup>) is demonstrably related to magmatic activity  
450 (Keir et al., 2009). This is also the case for the Eyasi rift and Kilimanjaro regions at similar depths (**Fig.13**),  
451 where connected networks of volatile-bearing basaltic melts well explain (**Fig.10b**) shallow high-  
452 conductivity anomalies ( $\geq 10^{-1}$  S.m<sup>-1</sup>;  $\leq 1$  GPa; Selway, 2015).

453 Importantly, it should be noted that the MT data are unable to resolve whether the anomaly crosses  
454 the Lithosphere-Asthenosphere Boundary (LAB). The MT profile reinterpreted in this study in light of our  
455 experimental results has limitations inherent to either the geological context or the geophysical method.  
456 The entire lower portions of the lithospheric mantle of the Tanzanian craton appear as a uniform  
457 conductor in the inversion model presented by Selway (2015). It is not possible to identify the lower  
458 electrical bound of the conductivity anomaly. If graphite acts as an important connector of the garnet  
459 grains, we would expect this mechanism to switch off upon the transition from the graphite to the  
460 diamond stability zone at a depth of  $\sim 150$  km, or most certainly at a depth above the LAB (**Fig.13**).

### 461 **5.4. Plume impingement and evolution of the cratonic lithosphere**

462 Zones with thin lithosphere are known to act as sinks for a buoyant mantle plume (e.g. Sleep, 1997). In  
463 particular, numerical modelling of plume-lithosphere interactions in the East African rift system shows that  
464 the mantle plume is deflected by the thick root of the Tanzanian craton and is preferentially channeled  
465 towards the neighboring mobile belt (Mozambique Belt), characterized by a thinner lithosphere (e.g.  
466 Koptev et al., 2016). Spatial variations in the lithospheric geotherm associated with plume impingement  
467 would induce lithospheric deformations around the craton (Koptev et al., 2018). However, our results,  
468 together with other recent studies (e.g. Muirhead et al., 2020) highlight deep metasomatism of the  
469 Tanzanian craton, which would mean that the lateral flow near the LAB is not incompatible with a  
470 significant incorporation of plume elements towards the deep cratonic lithosphere.



471 Although fertilization processes may depend on geological settings and would not necessarily require  
472 the action of a mantle plume (Griffin et al., 2009; O'Reilly & Griffin, 2013), we would favor the plume  
473 impingement interpretation in the context of the East African Rift. The increase of the fraction of garnet  
474 pyroxenites within the cratonic root would induce an increase in density, which could contribute in  
475 lithospheric delamination (e.g. Foley, 2008; Ye et al., 2018; Hu et al., 2018; Celli et al., 2020). Furthermore,  
476 lithospheric delamination can open asthenospheric windows responsible for delamination-induced  
477 magmatism (Kay & Kay, 1993), prone to act as positive feedback for root metasomatism and associated  
478 densification.

479 It is likely that garnet pyroxenites exist in the deep lithospheric mantle of both the Tanzanian Craton  
480 and Mozambique Belt, as illustrated on **Fig.13**, but these garnet pyroxenites need to be connected to  
481 significantly impact the electrical conductivity. Considering an iterative interaction for millions of years  
482 between plume-derived melts/fluids and rocks of the cratonic root and a lateral percolation flow towards  
483 the Mozambique Belt, the formation of well interconnected high-conductivity pathways is more likely  
484 within the cratonic root. We propose that the observed electrical anomaly could be the signature of a  
485 critical state of a cratonic root between stability and disruption.

## 486 **Conclusions**

487 Electrical conductivity measurements at high pressures and temperatures on dunite and pyroxenite  
488 xenoliths from Tanzania allow reproducing the high conductivity anomaly of the deep Tanzanian Craton.  
489 High electrical conductivity values are associated with connected networks of garnet-rich rocks, with  
490 natural H contents limited to values  $< 0.1$  vol.%. The experiments indicate that the conductive rocks most  
491 likely consist of garnet pyroxenites, in which both garnet and pyroxenes can bear significant H amounts.

492 Once garnet becomes stable in fertile mantle rocks ( $> 60$  km, 1.7 GPa), it can nucleate at grain  
493 boundaries (e.g. this study; Henjes-Kunst & Altherr, 1992) or as connected reaction rims (e.g. Vrijmoed et  
494 al., 2013), forming the backbone of a conductive network. At 3 GPa, such garnet-rich networks increase  
495 conductivity by a factor of 100 regardless of temperature. Numerical models show that the observed low  
496 ( $< 10^{-2} \text{ Sm}^{-1}$ ) and high ( $> 10^{-1} \text{ Sm}^{-1}$ ) conductivity values are best explained by low and high degrees of garnet  
497 connectivity, respectively. Such high electrical conductivities in cratonic roots can be explained by the  
498 presence of connected garnet clusters or garnet pyroxenites, suggesting mantle fertilization.

499 In all likelihood, the high electrical conductivity in the root of the Tanzanian Craton highlights current  
500 plume impingement that has lasted for millions of years, consistently with the up-to-date knowledge on  
501 the area. Deep melts/fluids would have iteratively percolated and fossilized, progressively increasing the

502 amount and connectivity of electrically conductive rocks within the deep lithosphere. Although our results  
503 are consistent with long-term craton stability, the garnet-rich network likely results from continuous  
504 metasomatism due to plume impingement and might represent an unstable structure prior to loss of  
505 cratonic lithosphere.

## 506 **Acknowledgments**

507 We thank Rong Zhang and Danielle Shields for assistance in the laboratory, Rob Evans (WHOI) for key  
508 discussions on magnetotellurics, Christian Chopin for the constructive discussion on mineral identification  
509 and stability conditions, Xin Zhong and Damien Deldicque for key advices and explanations about Raman  
510 data acquisition and interpretation, and Timm John for providing key references about garnet connectivity  
511 in natural rocks. This work is partly funded by the *Alexander von Humboldt* Foundation and the Labex  
512 *VOLTAIRE* (Université d'Orléans). We acknowledge SIO-PEPL for the facility and Kurt Leinenweber for  
513 providing cell assemblies; use of the COMPRES Cell Assembly Project was supported by COMPRES under  
514 NSF Cooperative Agreement EAR 1661511. TPF thanks Jonathan Souders (UCSD – SiO IGPP) for the  
515 technical expertise on electrical circuits, Sabine Faulhaber (UCSD Nanoengineering Dept.) for her help with  
516 scanning electron microscopy, Isabel Rivera-Collazo (UCSD Anthropology Dept.– SIO) for her help with the  
517 particle size analyzer and Sean Curran (UCSD – SiO GRD) for his help with pixel counting (garnet fraction  
518 estimate).

## 519 **Authors contributions**

520 EJC provided the xenoliths powders, analyzed their mineralogy and performed the SIMS  
521 measurements. TPF performed the experiments, collected the electrical data, microstructural  
522 observations and Raman data and prepared the figures. The authors discussed the results, draw  
523 interpretations and perspectives and wrote the paper.

524

525 **Tables**526 **Table 1: Compositions (XRF) of the Tanzanian and Chinese rocks on which electrical data exist.**

Location	Northern Tanzania					China		
	Engorora			Lashaine		Dengpa, Tibet	Wanquan, HeBei	
Sampling	Xenoliths			Xenoliths		Outcrop	Xenoliths	
Nature	Dunite ENG-8	Pyroxenite ENG-7	Host lava	Lherzolite	Host lava	Dunite	Lherzolite	Pyroxenite
Major elements oxides (wt.%)								
SiO <sub>2</sub>	39.94	51.40	43.09	44.37	39.44	41.36	44.79	48.08
TiO <sub>2</sub>	0.16	0.57	2.47	0.08	2.37	0.01	0.08	0.62
Al <sub>2</sub> O <sub>3</sub>	0.35	2.87	5.71	2.44	5.84	0.12	2.31	6.25
Cr <sub>2</sub> O <sub>3</sub>	0.12	0.37	0.39	0.48	0.11	<i>n.d.</i>	<i>n.d.</i>	<i>n.d.</i>
FeOT	13.56	8.82	11.56	7.27	12.88	3.86	8.14	9.24
Fe <sub>2</sub> O <sub>3</sub>	<i>n.d.</i>	<i>n.d.</i>	<i>n.d.</i>	0.85	9.21	0.34	1.89	3.04
FeO	<i>n.d.</i>	<i>n.d.</i>	<i>n.d.</i>	6.42	4.59	3.52	6.25	6.20
MnO	0.19	0.18	0.20	0.09	0.17	0.04	0.13	0.15
MgO	43.87	17.66	18.71	42.14	17.67	52.34	40.72	17.27
CaO	0.91	17.09	12.35	1.45	12.24	0.95	2.26	15.43
Na <sub>2</sub> O	0.00	0.51	1.24	0.25	1.97	0.01	0.07	0.56
K <sub>2</sub> O	0.03	0.06	0.75	0.08	0.99	0.02	0.02	0.02
P <sub>2</sub> O <sub>5</sub>	0.24	0.17	0.51	0.05	0.81	0.01	0.01	0.02
H <sub>2</sub> O <sup>+</sup>	<i>n.d.</i>	<i>n.d.</i>	0.74	0.39	0.8	0.46	1.28	1.58
H <sub>2</sub> O <sup>-</sup>	<i>n.d.</i>	<i>n.d.</i>	<i>n.d.</i>	0.18	2.26	<i>n.d.</i>	<i>n.d.</i>	<i>n.d.</i>
CO <sub>2</sub>	<i>n.d.</i>	<i>n.d.</i>	0.74	0.25	1.41	0.08	0.13	0.21
Total	99.38	99.69	96.98	99.52	99.88	98.72	98.53	97.64
Mg#	0.85	0.78	0.74	0.85	0.71	0.961	0.899	0.455
Ref.	Chin, 2018			Dawson et al., 1970		Wang et al., 2008		

527

528 **Table 2: Composition and H content of the Engorora xenoliths.**

	Modal mineralogy cpx:opx:ol:chr	Average cpx H (ppm H <sub>2</sub> O)	1 $\sigma$ *	Average opx H (ppm H <sub>2</sub> O)	1 $\sigma$ *	Average olivine H (ppm H <sub>2</sub> O)	1 $\sigma$ *	Whole-rock Mg#	Whole-rock reconstructed (ppm H <sub>2</sub> O)
ENG14**	14:tr:85:1	64	22	not present	n/a	16	(1 grain)	84	22
ENG12	46:tr:52:2	124	42	not present	n/a	35	(1 grain)	82	75
ENG7	87:11:2:tr	273	62	163	50	not analysed	n/a	78	255

cpx = clinopyroxene, opx = orthopyroxene, ol = olivine, chr = chromite, tr = trace;  
\*1 $\sigma$  is the standard deviation of all spot measurements per xenolith;  
\*\*ENG14 is petrologically and texturally very similar to ENG8 (dunite used in this study).

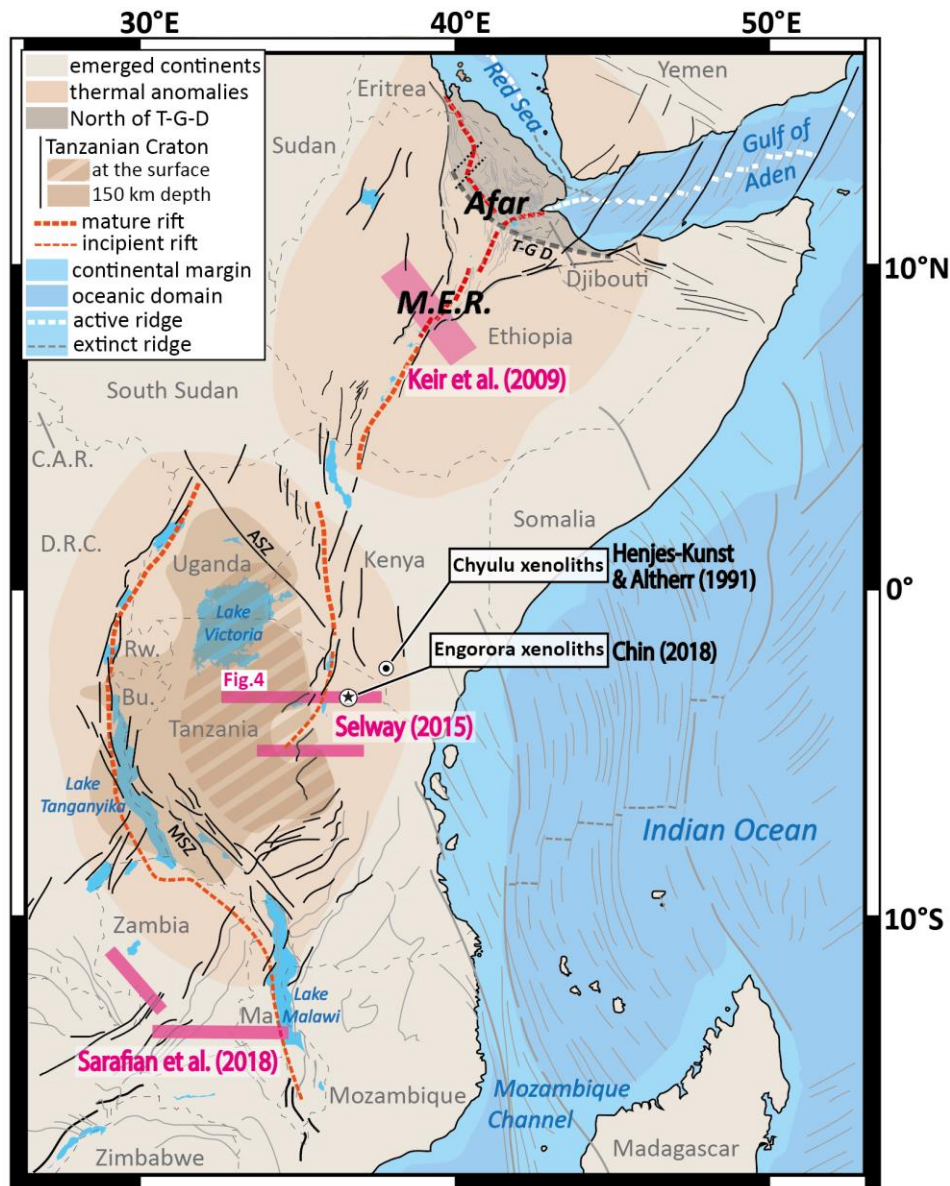
529 Modal mineralogies were calculated by least-squares inversion of the whole-rock and average mineral major  
530 element compositions. For details on water content determination using secondary ion mass spectrometry  
531 (SIMS), see the **Supplementary Information (section 1.3)**. It should be noted that Raman spectrometry identifies  
532 a H amount in ENG8 larger than ENG7, which suggests that H in ENG8 (and most probably ENG14) would be  
533 preferentially localized at grain boundaries or tiny grains whereas SIMS measurements are performed on grain  
534 interiors (spot = 8  $\mu$ m).

535

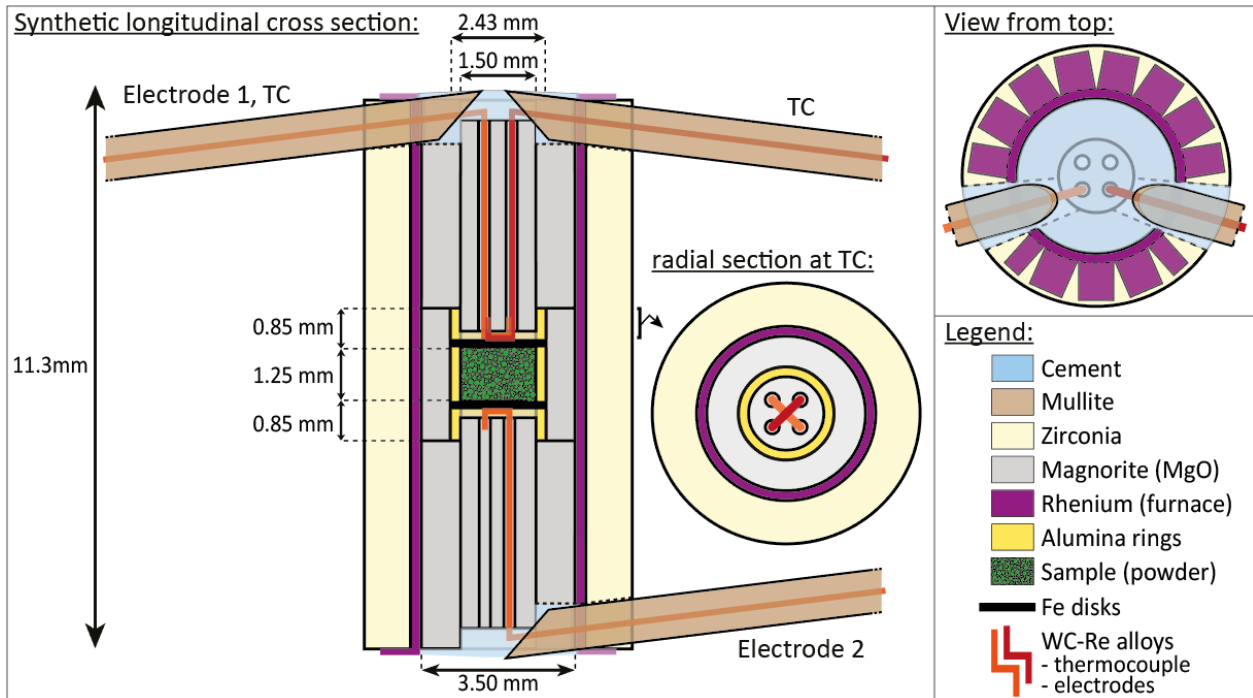
536 **Table 3: Summary of the experiments.**

Run	Starting material	P (GPa)	T <sub>max</sub> (°C)	Hydrogen	carbon	Microstructural observations
BB-244	ENG7: pyroxenite xenolith powder	1.5	1403	~200 ppm H <sub>2</sub> O	10-100 ppm CO <sub>2</sub> ; < 0.1 wt.% graphite	(sub)micrometric spinel crystals localized in melt pockets.
BB-253		3.0	750			Submicrometric garnets at grain boundaries; no melting.
BB-246			1400			(sub)micrometric garnet networks.
BB-254			1575			crystallized melt pockets containing Fe-rich dendrites (melting of the electrodes).
BB-238	ENG8: dunite xenolith powder	1.5	1342	~25 ppm H <sub>2</sub> O		melt wetting triple junctions.
BB-247		3.0	1449			some garnet grains, not connected; few quenched silicate melt pockets.

537 The H contents come from SIMS measurements on olivine and pyroxene crystals from the studied xenoliths,  
538 presented in the **Supplementary Information**. For detailed microstructural observations, see **Fig.5-9**.

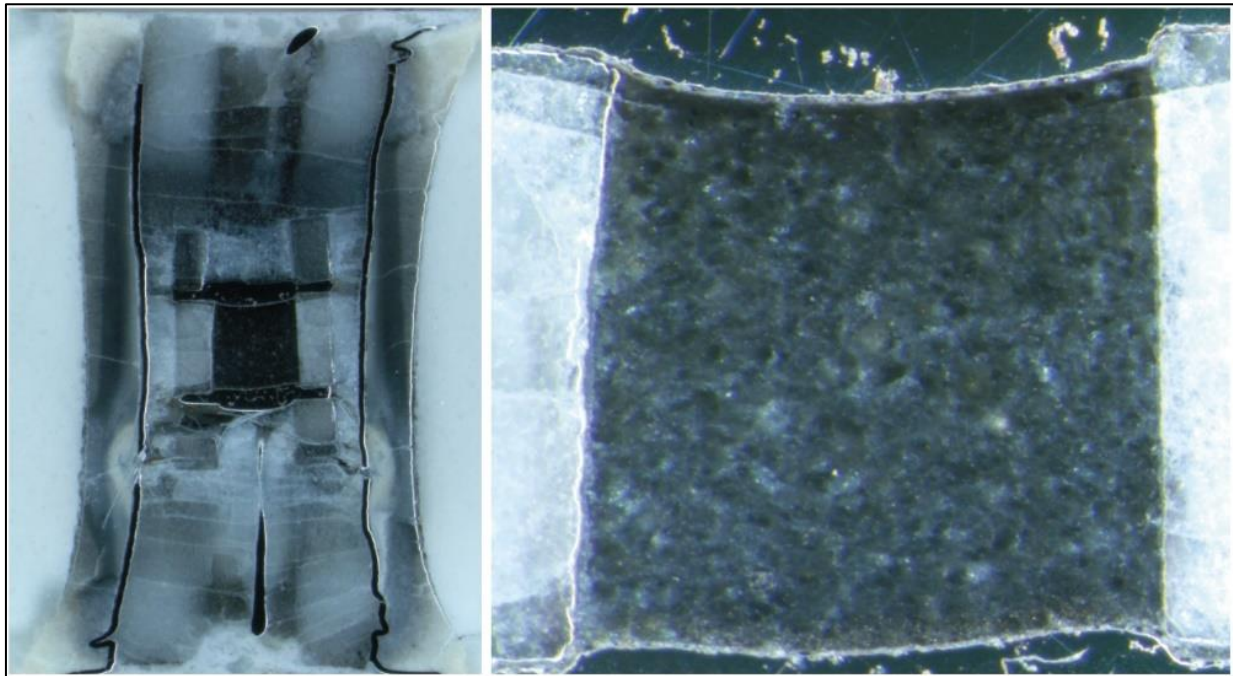


540  
 541 **Figure 1: Synthetic map of the East African Rift**, adapted from Chorowicz (2005), Sarafian et al. (2018)  
 542 and Lemna et al. (2019), with oceanic fabric from Phethean et al. (2016). The limits of the Tanzanian  
 543 Craton are from Koptev et al. (2016). The Blackstar indicates the origin of the Engorora xenoliths (Chin,  
 544 2018) used as starting material in this study; the black dot locates the origin of the Chyulu xenoliths  
 545 (Henjes-Kunst & Altherr, 1992). Pink segments locate the profiles of previous magnetotelluric studies  
 546 across the Tanzanian (Selway, 2015) and Zambian (Sarafian et al., 2018) incipient rifts, and across the  
 547 Main Ethiopian Rift (M.E.R.; Keir et al., 2009). Legend: ASZ: Aswa Shear Zone; MFZ: Mugheze Fracture  
 548 Zone; T.G.D. = Tendaho-Goba'ad Discontinuity. Countries abbrv.: Bu. = Burundi; C.A.R. = Central African  
 549 Republic; D.R.C. = Democratic Republic of the Congo; Ma. = Malawi; Rw. = Rwanda.



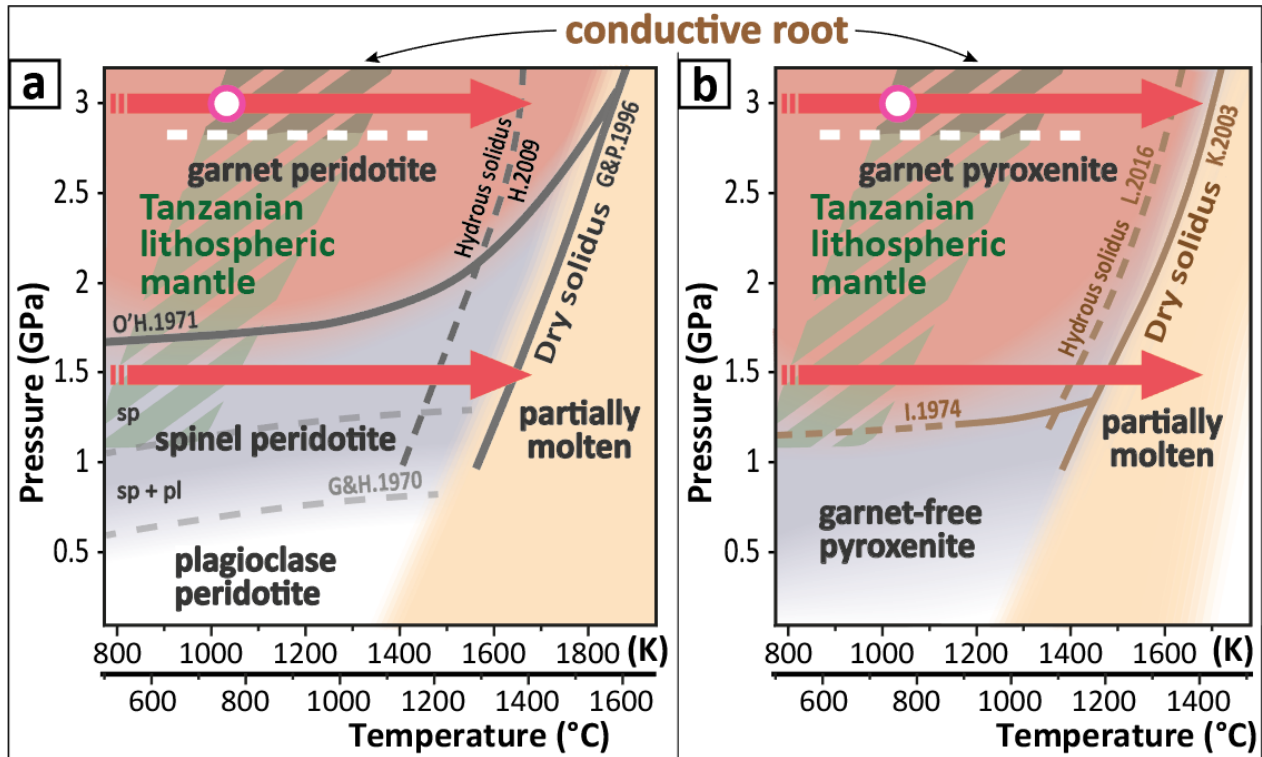
550  
551  
552  
553

**Figure 2: Experimental assembly.** Synthetic sketch of the 14/8 COMPRES electrical assembly. Experiment BB-238 was performed using a 4-electrodes assembly (4 wires), which consist of a “symmetrical” assembly with 2 thermocouples.



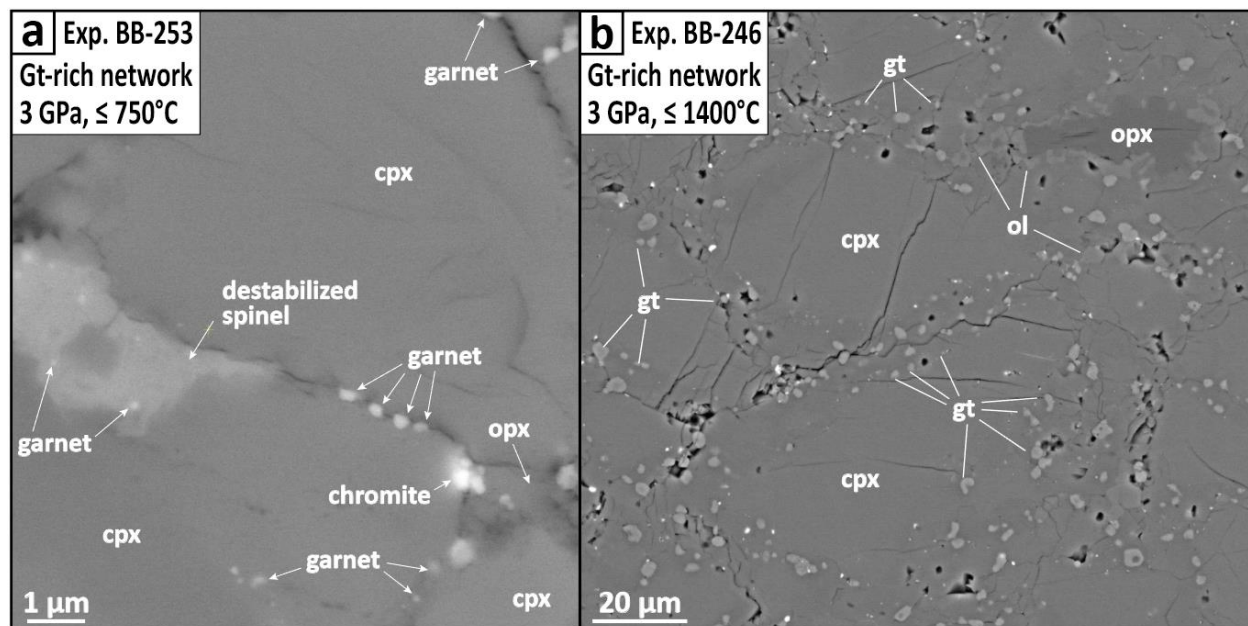
554  
555  
556  
557

**Figure 3: Recovered assembly.** Run BB-246 (see Table 3): clinopyroxenite ENG7 pressurized to 3 GPa at temperatures up to 1400 °C. Microstructural observations are shown in **Fig.5b** and **Fig.7**. Electrical data are given in **Fig.10**.



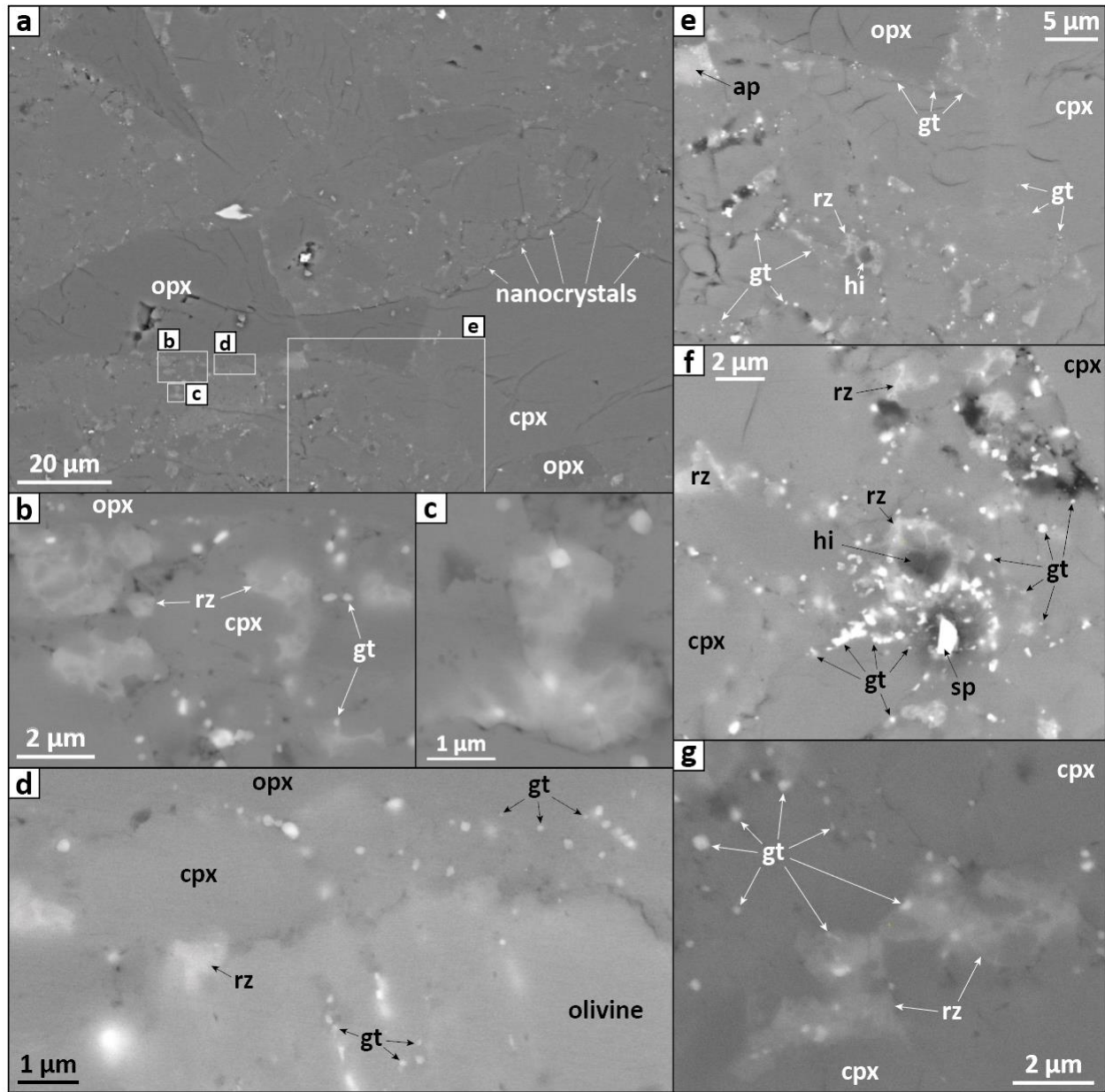
558  
 559 **Figure 4: Experimental conditions and paragenesis expected from thermodynamics.** Pressure-  
 560 temperature diagram summarizing experimental conditions (red arrows) and highlighting the garnet  
 561 stability field in mantle rocks (**a** = peridotites; **b** = pyroxenites) and the Tanzanian lithospheric mantle.  
 562 The white dot indicates the maximum temperature (750°C) during experiment BB-253 (ENG7, 3 GPa;  
 563 no elec. data). The white dashed line indicates the minimum pressure expected at  $\approx$  100 km depth (i.e.  
 564 top of the conductive anomaly = craton root) Legend: pl = plagioclase; sp = spinel. Ref: G&P.1996 =  
 565 Gudfinnsson & Presnall (1996); H2009: Hirschmann et al. (2009); I.1974 = Irving (1974); K.2003 =  
 566 Kogiso et al. (2003); L.2016: Lambart et al. (2016); O'H.1971 = O'Hara et al. (1971); G&H.1970 = Green  
 567 & Hibberson (1970).





568  
 569 **Figure 5: High conductivity due to hydrous Fe-rich garnet networks at high-pressure.** **a:** Backscattered  
 570 electron image (BSE) of an experimental garnet network (3 GPa, quench at 750°C), showing a destabilized  
 571 spinel and submicrometric garnets crystallizing along grain boundaries; **b:** High-temperature garnet-rich  
 572 channels (3 GPa, quench at 1400°C), showing larger garnet grains due to enhanced diffusion. For additional  
 573 BSE images, see **Fig.6** to **9**. For EDS mapping, see **Fig.S5** and **S6**. During the spinel-garnet transition, Fe  
 574 diffuses from destabilized spinel and oxides, while Al, Ca and OH are consumed from the surrounding  
 575 minerals. Abbrev.: cpx = clinopyroxene; gt: garnet; ol = olivine; opx = orthopyroxene.

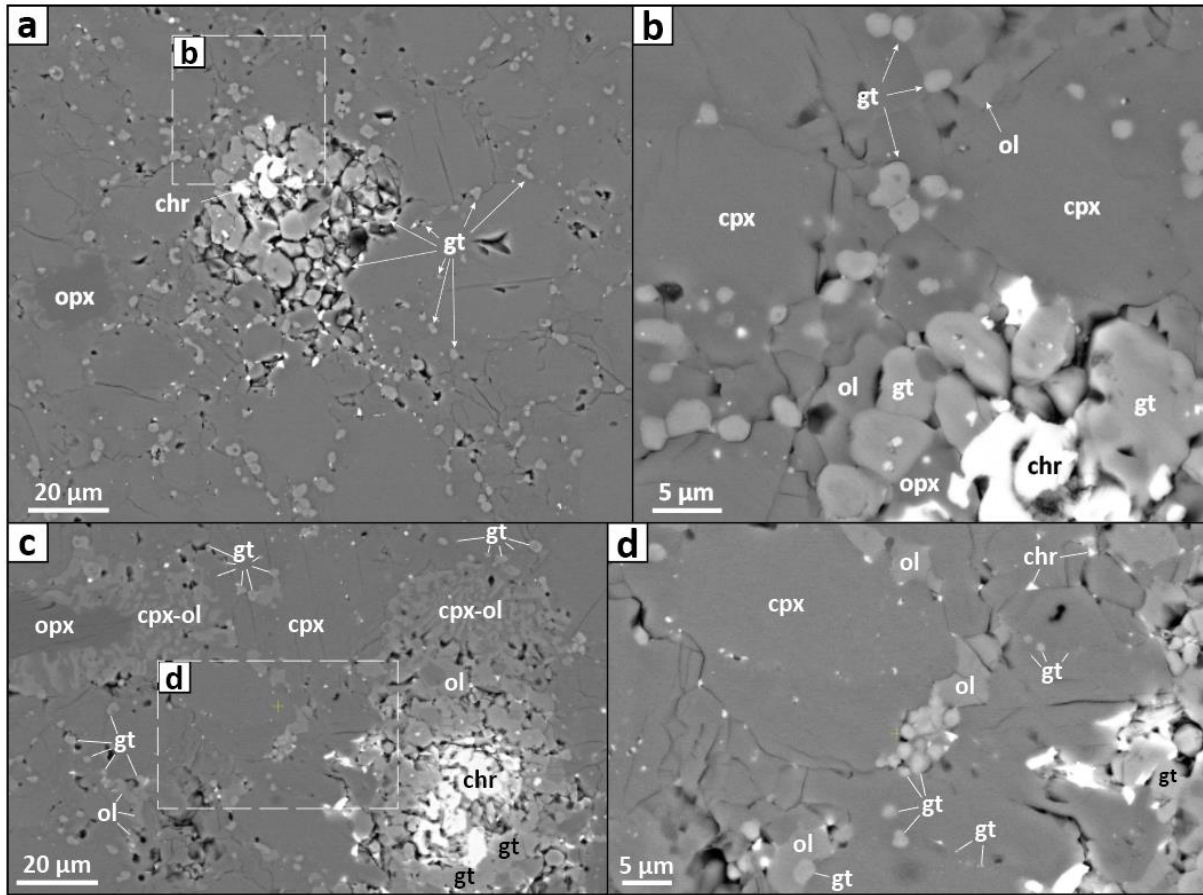




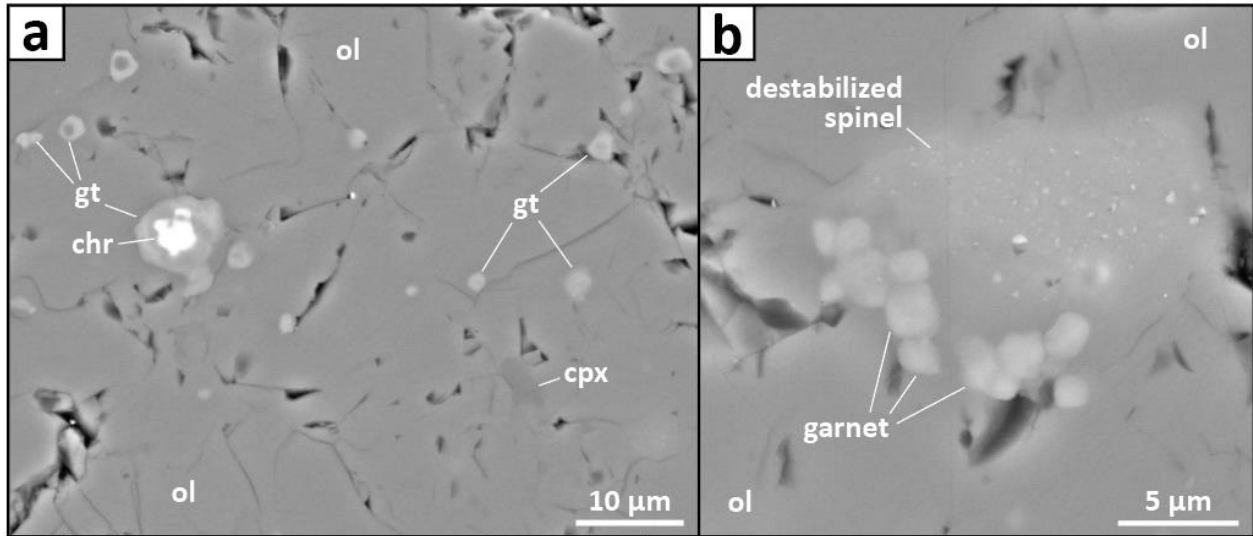
576

577 **Figure 6: Additional BSE images on sample BB-253 (pyroxenite, 3 GPa, 750°C).** Supplement of Fig.5a.

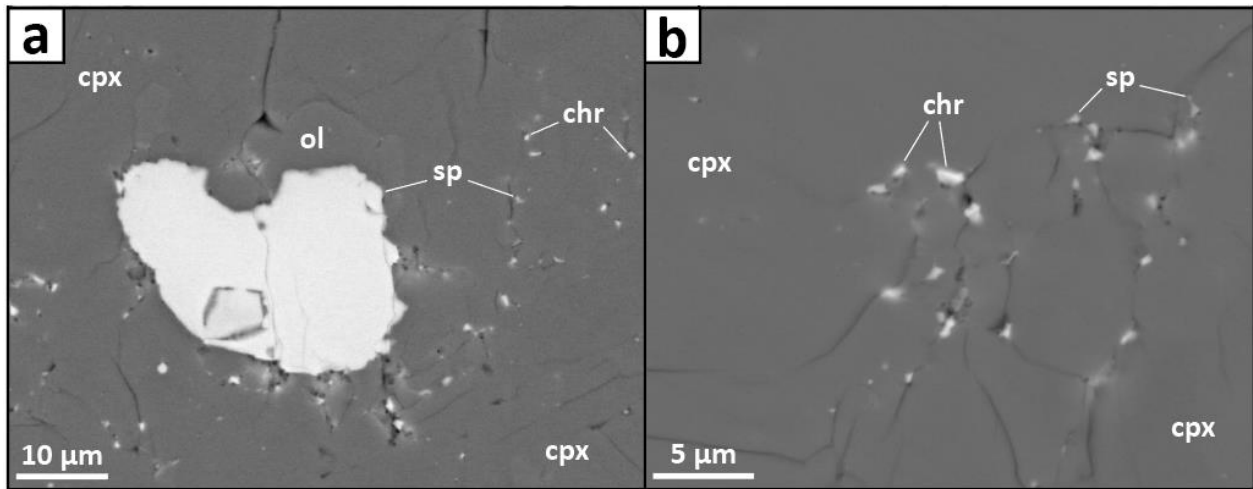
578 Abbrev.: cpx = clinopyroxene; gt: garnet; hi = hibonite; opx = orthopyroxene; rz = reaction zone; sp = spinel.



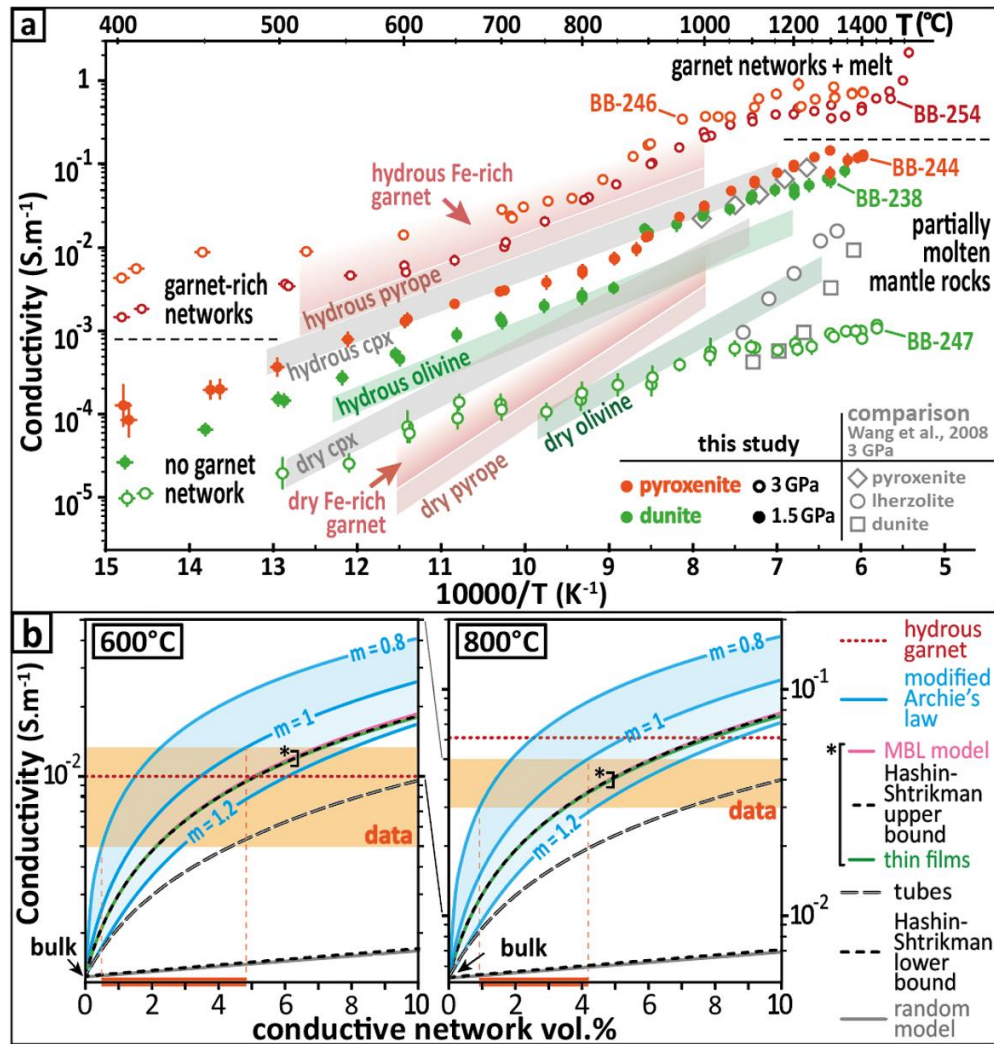
579  
 580 **Figure 7: Additional BSE images on sample BB-246 (pyroxenite, 3 GPa, 1400°C).** Supplement of Fig.5b.  
 581 Networks of micrometric garnet crystals develop along grain boundaries throughout the sample. Larger  
 582 garnet grains grow at the expense of Al-rich spinel, while chromite crystals remain stable. In addition,  
 583 symplectites develop between opx, cpx and accessory minerals, which highlight metamorphic reactions.  
 584 Abbrev.: chr: chromite; cpx = clinopyroxene; ol = olivine; opx = orthopyroxene; gt = garnet.  
 585



586  
 587 **Figure 8: Additional BSE images on sample BB-247 (dunite, 3 GPa, 1449°C).** Micrometric garnet grains  
 588 grow only locally, in the vicinity of minor metal oxides (a) and destabilized spinel (b). Abbrev.: cpx =  
 589 clinopyroxene; ol = olivine; chr: chromite; gt = garnet.



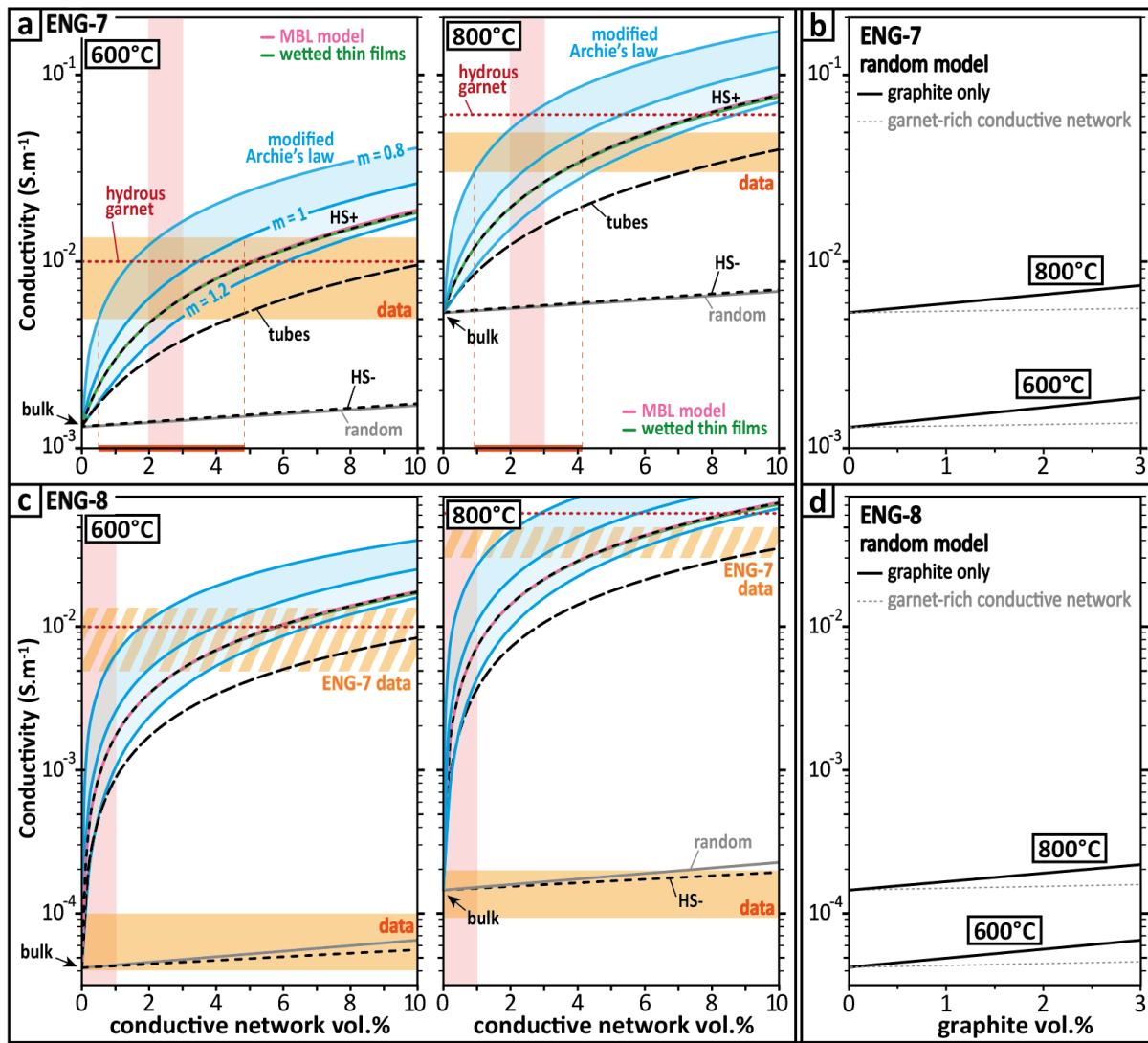
590  
 591 **Figure 9: Additional BSE images on sample BB-244 (pyroxenite, 1.5 GPa, 1403°C).** No garnet is observed.  
 592 Both chromite and Al-rich spinel, originating from the xenolith powder, remain stable. Abbrev.: ol = olivine;  
 593 cpx = clinopyroxene; chr: chromite; sp = spinel.



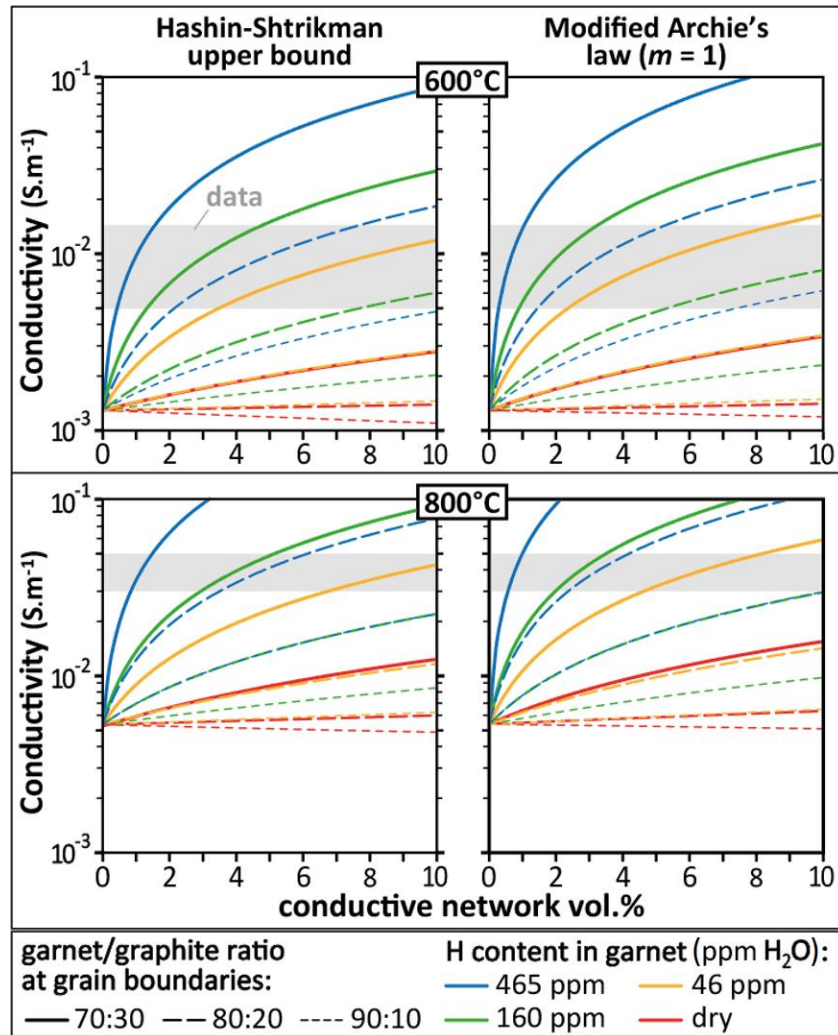
594  
 595 **Figure 10: Experimental results and comparison with models.** (a) Electrical conductivity versus reciprocal  
 596 temperature for the Engorora xenoliths, at 1.5 GPa (solid circles) and 3 GPa (open circles). For comparison,  
 597 the green, grey and red shades correspond to electrical conductivity values for dry ( $X_{\text{Fe}} = 0.1$ , 6-19 GPa;  
 598 Yoshino et al., 2012) and hydrous olivine (465 ppm  $\text{H}_2\text{O}$ ; Gardés et al., 2014), dry and hydrous (375 ppm  
 599  $\text{H}_2\text{O}$ ) clinopyroxene (Yang et al., 2011) and dry pyrope ( $\text{Py}_{73}\text{-Alm}_{14}\text{-Gr}_{13}$ , 3 GPa; Dai et al., 2012) and  
 600 hydrous pyrope (465 ppm  $\text{H}_2\text{O}$ ; 3 GPa; Dai et al., 2012). (b) Conductivity simulations based on several  
 601 models and compared to the experimental data at 600 and 800°C, i.e. before any melting. Grain-boundary  
 602 network: 80:20 garnet/graphite circuit ( $\sim 0.1$  wt.% carbon). The orange box indicates the experimental  
 603 electrical data at a given temperature (uncertainty range) extracted from Fig.10a, for comparison with the  
 604 models (listed on the right side). The thick red line on x axis is the volume fraction of connected conductive  
 605 network as deduced/extrapolated from the comparison between the electrical data and the connectivity  
 606 models. For details on the models, see the SI. For additional simulations, see Fig.11 and Fig.12. The even  
 607 higher conductivity observed in this study is attributed to hydrogarnet-rich Fe-rich pyrope. A summary of  
 608 experimental conditions and results is provided in Fig.4 and Table 3, including experiment BB-253 (ENG7,



609 P = 3 GPa, T ≤ 750°C), for which no electrical data was recorded. The parameters and different models are  
 610 provided in **Table S3** to **Table S4**.  
 611

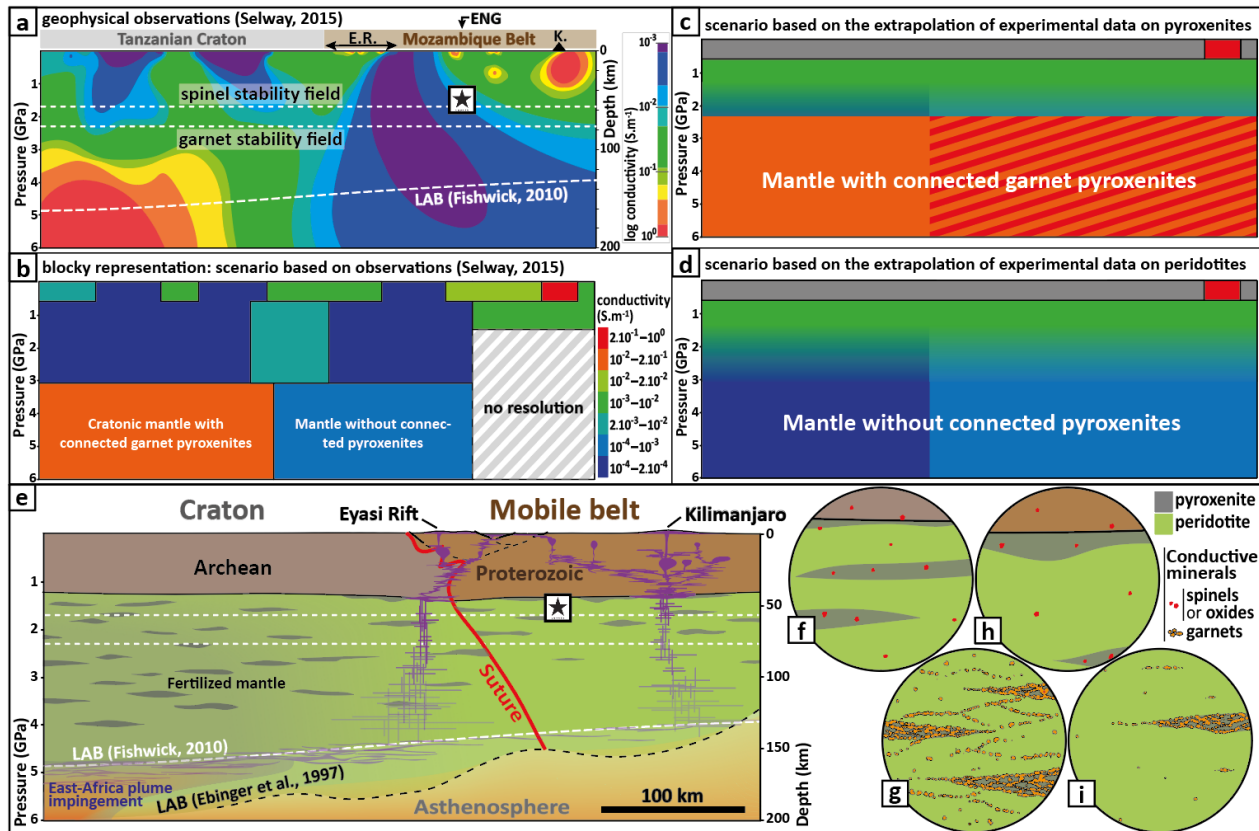


612  
 613 **Figure 11: Conductivity simulations considering various geometries.** Calculations for ENG7 (a-b)  
 614 and ENG8 (c-d) at 600 and 800°C (no partial melting involved). The parameters considered for the  
 615 models are listed in **Table S3**, and the formula are detailed in **Table S4**. Here the H amount in  
 616 garnet is assumed to be 465 ppm. See **Fig.S6** for other H amounts. A table of values is provided in  
 617 **Table S5**.



618  
619  
620  
621  
622  
623

**Figure 12: Effect of garnet/graphite ratio and H content on conductivity.** Detailed simulations for the Hashin-Shtrikman upper bound (left) and the modified Archie's law (right) at 600 and 800°C. Simulation on ENG7 composition, compared to data (grey). The parameters used for the models are listed in **Table S3**. The formula are detailed in **Table S4**, with a table of values provided in **Table S5**.



624  
 625 **Figure 13: Geophysical and geological implications.** (a) Results of the magnetotelluric survey (redrawn  
 626 after Selway, 2015) located in Fig.1, with depth of the spinel-garnet transition (O’Hara et al., 1971) and  
 627 LAB (Fishwick, 2010); (b) Block representation of the best fit from connectivity data inversions (Selway,  
 628 2015); (c) block representation from the extrapolation of the experiments on pyroxenites; (d) block  
 629 representation from the extrapolation of the experiments on pyroxenites; (e) Geological interpretation,  
 630 with up-to-date topography (Wichura et al., 2011), Moho depth (Last et al., 1997; Julià et al., 2005),  
 631 Lithosphere-Asthenosphere Boundary (LAB; Ebinger et al., 1997; Fishwick, 2010) and Eyasi suture zone  
 632 (Ebinger et al., 1997) (vertical exaggeration x2). (f) uppermost cratonic mantle at 1.5 GPa; (g) deep cratonic  
 633 lithosphere containing a network of connected garnets; (h) uppermost mantle of the Mozambique Belt;  
 634 (i) with limited garnet connectivity. The Blackstar indicates the approximate origin of the Engorora  
 635 xenoliths (Chin, 2018), i.e. 0.9-1.7 GPa (Fig.4). Legend: ENG = Engorora; E.R = Eyasi Rift; K = Kilimanjaro.

636 **References**

- 637 1. Aines, R. D. & Rossman, G. R. 1984. Water content of mantle garnets. *Geology* **12**(12), 720-723.
- 638 2. Bizimis, M. & Peslier, A. H. 2015. Water in Hawaiian garnet pyroxenites: Implications for water  
639 heterogeneity in the mantle. *Chemical Geology* **397**, 61-75.
- 640 3. Celli, N. L., Lebedev, S., Schaeffer, A. J. & Gaina, C. 2020. African cratonic lithosphere carved by  
641 mantle plumes. *Nature Communications* **11**(1), 1-10.
- 642 4. Chin, E. J. 2018. Deep crustal cumulates reflect patterns of continental rift volcanism beneath  
643 Tanzania. *Contributions to Mineralogy & Petrology* **173**(10), 85.
- 644 5. Chin, E. J., Soustelle, V. & Liu, Y. 2020. An SPO-induced CPO in composite mantle xenoliths correlated  
645 with increasing melt-rock interaction. *Geochimica et Cosmochimica Acta* **278**, 199-218.
- 646 6. Chorowicz, J. 2005. The east African rift system. *Journal of African Earth Sciences* **43**(1-3), 379-410.
- 647 7. Clerc, J. P., Giraud, G., Alexander, S. & Guyon, E. 1979. Conductivity of a mixture of conducting and  
648 insulating grains: Dimensionality effects. *Physical Review B*. **22** (5): 2489-2494.
- 649 8. Dai, L., Li, H., Hu, H., Shan, S., Jiang, J. & Hui, K. 2012. The effect of chemical composition and oxygen  
650 fugacity on the electrical conductivity of dry and hydrous garnet at high temperatures and pressures.  
651 *Contributions to Mineralogy & Petrology* **163**(4), 689-700.
- 652 9. Dai, L. & Karato, S. I. 2009. Electrical conductivity of orthopyroxene: Implications for the water  
653 content of the asthenosphere. *Proceedings of the Japan Academy, Series B* **85**(10), 466-475.
- 654 10. Dawson, J. B., Powell, D. G. & Reid, A. M. 1970. Ultrabasic xenoliths and lava from the Lashaine  
655 volcano, northern Tanzania. *Journal of Petrology* **11**(3), 519-548.
- 656 11. Deldicque, D., Rouzaud, J. N., Vandevelde, S., Medina-Alcaide, M. Á., Ferrier, C., Perrenoud, C. ... &  
657 Cabanis, M. 2023. Effects of oxidative weathering on Raman spectra of charcoal and bone chars:  
658 consequences in archaeology and paleothermometry. *Comptes Rendus. Géoscience* **355**(G1), 1-22.
- 659 12. Doucet, L. S., Peslier, A. H., Ionov, D. A., Brandon, A. D., Golovin, A. V., Goncharov, A. G. &  
660 Ashchepkov, I. V. 2014. High water contents in the Siberian cratonic mantle linked to metasomatism:  
661 An FTIR study of Udachnaya peridotite xenoliths. *Geochimica et Cosmochimica Acta* **137**, 159-187.
- 662 13. Duba, A. G. & Shankland, T. J. 1982. Free carbon & electrical conductivity in the Earth's mantle.  
663 *Geophysical Research Letters* **9**(11), 1271-1274.
- 664 14. Ebinger, C., Djomani, Y. P., Mbede, E., Foster, A. & Dawson, J. B. 1997. Rifting archaean lithosphere:  
665 the Eyasi-Manyara-Natron rifts, East Africa. *Journal of the Geological Society* **154**(6), 947-960.
- 666 15. Evans, R. L., Jones, A. G., Garcia, X., Muller, M., Hamilton, M., Evans, S., ... & Hutchins, D. 2011.  
667 Electrical lithosphere beneath the Kaapvaal craton, southern Africa. *JGR Solid Earth* **116**(B4).
- 668 16. Ferrand, T. P. 2020. Conductive channels in the deep oceanic lithosphere could consist of garnet  
669 pyroxenites at the fossilized lithosphere–asthenosphere boundary. *Minerals* **10**(12), 1107.
- 670 17. Fisher, J. C. 1951. Calculation of diffusion penetration curves for surface and grain boundary  
671 diffusion. *Journal of Applied Physics* **22**(1), 74-77.
- 672 18. Fishwick, S. 2010. Surface wave tomography: imaging of the lithosphere–asthenosphere boundary  
673 beneath central and southern Africa? *Lithos* **120**(1-2), 63-73.
- 674 19. Foley, S. F. 2008. Rejuvenation and erosion of the cratonic lithosphere. *Nature geoscience* **1**(8), 503-  
675 510.
- 676 20. Frost, D. J. & McCammon, C. A. 2008. The redox state of Earth's mantle. *Annual Review of Earth &*  
677 *Planetary Sciences* **36**, 389-420.
- 678 21. Gardés, E., Gaillard, F. & Tarits, P. 2014. Toward a unified hydrous olivine electrical conductivity law.  
679 *Geochemistry, Geophysics, Geosystems* **15**(12), 4984-5000.



- 680 22. Glover, P. W., Hole, M. J. & Pous, J. 2000. A modified Archie's law for two conducting phases. *Earth*  
681 *& Planetary Science Letters* **180**(3-4), 369-383.
- 682 23. Green, D. H. & Hibberson, W. 1970. The instability of plagioclase in peridotite at high pressure. *Lithos*  
683 **3**(3), 209-221.
- 684 24. Griffin, W. L. & O'Reilly, S. Y. 2007. The earliest subcontinental lithospheric mantle. *Developments*  
685 *in Precambrian Geology* **15**, 1013-1035.
- 686 25. Griffin, W. L., O'Reilly, S. Y., Afonso, J. C. & Begg, G. C. 2009. The composition and evolution of  
687 lithospheric mantle: a re-evaluation and its tectonic implications. *Journal of Petrology* **50**(7), 1185-  
688 1204.
- 689 26. Gudfinnsson, G. H. & Presnall, D. C. 1996. Melting relations of model lherzolite in the system CaO-  
690 MgO-Al<sub>2</sub>O<sub>3</sub>-SiO<sub>2</sub> at 2.4-3.4 GPa and the generation of komatiites. *Journal of Geophysical Research:*  
691 *Solid Earth* **101**(B12), 27701-27709.
- 692 27. Gueguen, Y. & Dienes, J. 1989. Transport properties of rocks from statistics and percolation.  
693 *Mathematical geology* **21**(1), 1-13.
- 694 28. Hales, A. L. 1969. A seismic discontinuity in the lithosphere. *Earth & Planetary Science Letters* **7**(1),  
695 44-46.
- 696 29. Henjes-Kunst, F. & Altherr, R. 1992. Metamorphic petrology of xenoliths from Kenya and northern  
697 Tanzania and implications for geotherms and lithospheric structures. *Journal of Petrology* **33**(5),  
698 1125-1156.
- 699 30. Hirschmann, M. M., Tenner, T., Aubaud, C. & Withers, A. C. 2009. Dehydration melting of nominally  
700 anhydrous mantle: The primacy of partitioning. *PEPI* **176**(1-2), 54-68.
- 701 31. Hirth, G. & Kohlstedt, D. 2003. Rheology of the upper mantle and the mantle wedge: A view from  
702 the experimentalists. *Geophysical Monograph – American Geophysical Union* **138**, 83-106.
- 703 32. Hu, J., Liu, L., Faccenda, M., Zhou, Q., Fischer, K. M., Marshak, S. & Lundstrom, C. 2018. Modification  
704 of the Western Gondwana craton by plume-lithosphere interaction. *Nature Geoscience* **11**(3), 203-  
705 210.
- 706 33. Irving, A. J. 1974. Geochemical and high-pressure experimental studies of garnet pyroxenite and  
707 pyroxene granulite xenoliths from the Delegate basaltic pipes, Australia. *Journal of Petrology* **15**(1),  
708 1-40.
- 709 34. James, D. E., Niu, F. & Rokosky, J. 2003. Crustal structure of the Kaapvaal craton and its significance  
710 for early crustal evolution. *Lithos* **71**(2-4), 413-429.
- 711 35. John, T., Scherer, E. E., Haase, K. & Schenk, V. 2004. Trace element fractionation during fluid-induced  
712 eclogitization in a subducting slab: trace element and Lu-Hf-Sm-Nd isotope systematics. *Earth &*  
713 *Planetary Science Letters* **227**(3-4), 441-456.
- 714 36. Jones, A. G., Fulla, J., Evans, R. L. & Muller, M. R. 2012. Water in cratonic lithosphere: Calibrating  
715 laboratory-determined models of electrical conductivity of mantle minerals using geophysical and  
716 petrological observations. *Geochemistry, Geophysics, Geosystems* **13**(6).
- 717 37. Julià, J., Ammon, C. J. & Nyblade, A. A. 2005. Evidence for mafic lower crust in Tanzania, East Africa,  
718 from joint inversion of receiver functions and Rayleigh wave dispersion velocities. *Geophysical*  
719 *Journal International* **162**(2), 555-569.
- 720 38. Keir, D., Bastow, I. D., Whaler, K. A., Daly, E., Cornwell, D. G. & Hautot, S. 2009. Lower crustal  
721 earthquakes near the Ethiopian rift induced by magmatic processes. *Geochemistry, Geophysics,*  
722 *Geosystems* **10**(6).
- 723 39. Keppler, H., Wiedenbeck, M. & Shcheka, S. S. 2003. Carbon solubility in olivine and the mode of  
724 carbon storage in the Earth's mantle. *Nature* **424**(6947), 414-416.

- 725 40. Kogiso, T., Hirschmann, M. M. & Frost, D. J. 2003. High-pressure partial melting of garnet pyroxenite:  
726 possible mafic lithologies in the source of ocean island basalts. *Earth & Planetary Science Letters*  
727 **216**(4), 603-617.
- 728 41. Koptev, A., Burov, E., Calais, E., Leroy, S., Gerya, T., Guillou-Frottier, L. & Cloetingh, S. 2016.  
729 Contrasted continental rifting via plume-craton interaction: Applications to Central East African Rift.  
730 *Geoscience Frontiers* **7**(2), 221-236.
- 731 42. Koptev, A., Calais, E., Burov, E., Leroy, S. & Gerya, T. 2018. Along-axis variations of rift width in a  
732 coupled lithosphere-mantle system, Application to East Africa. *Geophysical Research Letters* **45**(11),  
733 5362-5370.
- 734 43. Lambart, S., Baker, M. B. & Stolper, E. M. 2016. The role of pyroxenite in basalt genesis: Melt-PX, a  
735 melting parameterization for mantle pyroxenites between 0.9 and 5 GPa. *JGR Solid Earth* **121**(8),  
736 5708-5735.
- 737 44. Lanari, P. & Engi, M. 2017. Local bulk composition effects on metamorphic mineral assemblages.  
738 *Reviews in Mineralogy & Geochemistry* **83**(1), 55-102.
- 739 45. Last, R. J., Nyblade, A. A., Langston, C. A. & Owens, T. J. 1997. Crustal structure of the East African  
740 Plateau from receiver functions and Rayleigh wave phase velocities. *Journal of Geophysical*  
741 *Research: Solid Earth* **102**(B11), 24469-24483.
- 742 46. Lee, C. T. & Rudnick, R. L. 1999. Compositionally stratified cratonic lithosphere: petrology and  
743 geochemistry of peridotite xenoliths from the Labait tuff cone, Tanzania. In *Proceedings of the 7th*  
744 *international Kimberlite conference* (pp. 503-521).
- 745 47. Lemna, O. S., Stephenson, R. & Cornwell, D. G. 2019. The role of pre-existing Precambrian structures  
746 in the development of Rukwa Rift Basin, southwest Tanzania. *Journal of African Earth Sciences* **150**,  
747 607-625.
- 748 48. Liu, J., Pearson, D. G., Wang, L. H., Mather, K. A., Kjarsgaard, B. A., Schaeffer, A. J., ... & Armstrong,  
749 J. P. 2021. Plume-driven re-cratonization of deep continental lithospheric mantle. *Nature* **592**(7856),  
750 732-736.
- 751 49. Maldener, J., Hösche, A., Langer, K. & Rauch, F. 2003. Hydrogen in some natural garnets studied by  
752 nuclear reaction analysis and vibrational spectroscopy. *Physics & Chemistry of Minerals* **30**(6), 337-  
753 344.
- 754 50. Miller, K. J., Montési, L. G. & Zhu, W. L. 2015. Estimates of olivine-basaltic melt electrical conductivity  
755 using a digital rock physics approach. *Earth & Planetary Science Letters* **432**, 332-341.
- 756 51. Muirhead, J. D., Fischer, T. P., Oliva, S. J., Laizer, A., van Wijk, J., Currie, C. A., ... & Ebinger, C. J. 2020.  
757 Displaced cratonic mantle concentrates deep carbon during continental rifting. *Nature* **582**(7810),  
758 67-72.
- 759 52. O'Donnell, J., Adams, A., Nyblade, A., Mulibo, G. & Tugume, F. 2013. The uppermost mantle shear  
760 wave velocity structure of eastern Africa from Rayleigh wave tomography: Constraints on rift  
761 evolution. *Geophysical Journal International* **194**, 961-978.
- 762 53. O'Hara, M. J., Richardson, S. W. & Wilson, G. 1971. Garnet-peridotite stability and occurrence in  
763 crust and mantle. *Contributions to Mineralogy & Petrology* **32**(1), 48-68.
- 764 54. O'Reilly, S. Y. & Griffin, W. L. 2013. Mantle metasomatism. *Metasomatism and the chemical*  
765 *transformation of rock*, 471-533.
- 766 55. Patro, P. K. & Sarma, S. V. S. 2009. Lithospheric electrical imaging of the Deccan trap covered region  
767 of western India. *Journal of Geophysical Research: Solid Earth* **114**(B1).

- 768 56. Pearson, D. G., Boyd, F. R., Haggerty, S. E., Pasteris, J. D., Field, S. W., Nixon, P. H. & Pokhilenko, N.  
769 P. 1994. The characterisation and origin of graphite in cratonic lithospheric mantle: a petrological  
770 carbon isotope and Raman spectroscopic study. *Contributions to Mineralogy & Petrology* **115**(4),  
771 449-466.
- 772 57. Peslier, A. H., Schönbächler, M., Busemann, H. & Karato, S. I. 2017. Water in the Earth's interior:  
773 Distribution and origin. *Space Science Reviews* **212**(1), 743-810.
- 774 58. Phethean, J. J., Kalnins, L. M., van Hunen, J., Biffi, P. G., Davies, R. J. & McCaffrey, K. J. 2016.  
775 Madagascar's escape from Africa: A high-resolution plate reconstruction for the Western Somali  
776 Basin and implications for supercontinent dispersal. *Geochemistry, Geophysics, Geosystems* **17**(12),  
777 5036-5055.
- 778 59. Pommier, A. & Leinenweber, K. D. 2018. Electrical cell assembly for reproducible conductivity  
779 experiments in the multi-anvil. *American Mineralogist* **103**(8), 1298-1305.
- 780 60. Ridley, J. & Thompson, A. 1986. The role of mineral kinetics in the development of metamorphic  
781 microtextures. *Advances in physical geochemistry* **5**, 154-193.
- 782 61. Romano, C., Poe, B. T., Kreidie, N. & McCammon, C. A. 2006. Electrical conductivities of pyrope-  
783 almandine garnets up to 19 GPa and 1700 C. *American Mineralogist* **91**(8-9), 1371-1377.
- 784 62. Rudnick, R. L., McDonough, W. F. & Chappell, B. W. 1993. Carbonatite metasomatism in the northern  
785 Tanzanian mantle: petrographic and geochemical characteristics. *Earth & Planetary Science*  
786 *Letters* **114**(4), 463-475.
- 787 63. Sarafian, E., Evans, R. L., Abdelsalam, M. G., Atekwana, E., Elsenbeck, J., Jones, A. G. & Chikambwe,  
788 E. 2018. Imaging Precambrian lithospheric structure in Zambia using electromagnetic methods.  
789 *Gondwana Research* **54**, 38-49.
- 790 64. Sleep, N. H. 1997. Lateral flow and ponding of starting plume material. *Journal of Geophysical*  
791 *Research: Solid Earth* **102**(B5), 10001-10012.
- 792 65. Selway, K. 2015. Negligible effect of hydrogen content on plate strength in East Africa. *Nature*  
793 *Geoscience* **8**(7), 543-546.
- 794 66. Selway, K., Yi, J. & Karato, S-I. 2014. Water content of the Tanzanian lithosphere from  
795 magnetotelluric data: Implications for cratonic growth and stability. *Earth & Planetary Science*  
796 *Letters* **388**, 175-186.
- 797 67. Spear, F. S. 2017. Garnet growth after overstepping. *Chemical Geology* **466**, 491-499.
- 798 68. Takahashi, E. 1990. Speculations on the Archean mantle: missing link between komatiite and  
799 depleted garnet peridotite. *Journal of Geophysical Research: Solid Earth* **95**(B10), 15941-15954.
- 800 69. Vauchez, A., Dineur, F. & Rudnick, R. 2005. Microstructure, texture and seismic anisotropy of the  
801 lithospheric mantle above a mantle plume: insights from the Labait volcano xenoliths (Tanzania).  
802 *Earth & Planetary Science Letters* **232**(3-4), 295-314.
- 803 70. Vrijmoed, J. C., Austrheim, H., John, T., Hin, R. C., Corfu, F. & Davies, G. R. 2013. Metasomatism in  
804 the ultrahigh-pressure Svartberget garnet-peridotite (Western Gneiss Region, Norway): implications  
805 for the transport of crust-derived fluids within the mantle. *Journal of Petrology* **54**(9), 1815-1848.
- 806 71. Wang, D., Mookherjee, M., Xu, Y. & Karato, S. I. 2006. The effect of water on the electrical  
807 conductivity of olivine. *Nature* **443**(7114), 977-980.
- 808 72. Wang, D., Li, H., Yi, L. & Shi, B. 2008. The electrical conductivity of upper-mantle rocks: water content  
809 in the upper mantle. *Physics & Chemistry of Minerals* **35**(3), 157-162.
- 810 73. Wang, D., Karato, S. I. & Jiang, Z. 2013. An experimental study of the influence of graphite on the  
811 electrical conductivity of olivine aggregates. *Geophysical Research Letters* **40**(10), 2028-2032.

- 812 74. Wang, H., van Hunen, J. & Pearson, D. G. 2015. The thinning of subcontinental lithosphere: The roles  
813 of plume impact and metasomatic weakening. *Geochemistry, Geophysics, Geosystems* **16**(4), 1156-  
814 1171.
- 815 75. Wang, L., Liu, J., Xu, Q. H. & Xia, Q. K. 2022. Craton destruction induced by drastic drops in  
816 lithospheric mantle viscosity. *Earth & Space Science*, e2022EA002455.
- 817 76. Wang, L., Hitchman, A. P., Ogawa, Y., Siripunvaraporn, W., Ichiki, M. & Fuji-ta, K. 2014. A 3-D  
818 conductivity model of the Australian continent using observatory and magnetometer array data.  
819 *Geophysical Journal International*, **198**(2), 1143-1158.
- 820 77. Watson, H. C., Roberts, J. J. & Tyburczy, J. A. 2010. Effect of conductive impurities on electrical  
821 conductivity in polycrystalline olivine. *Geophysical Research Letters* **37**(2).
- 822 78. Watson, E. B. 1986. Immobility of reduced carbon along grain boundaries in dunite. *Geophysical*  
823 *Research Letters* **13**(6), 529-532.
- 824 79. Wichura, H., Bousquet, R., Oberhänsli, R., Strecker, M. R. & Trauth, M. H. 2011. The Mid-Miocene  
825 East African Plateau: a pre-rift topographic model inferred from the emplacement of the phonolitic  
826 Yatta lava flow, Kenya. *Geological Society, London, Special Publications* **357**(1), 285-300.
- 827 80. Yang, X., Keppler, H., McCammon, C., Ni, H., Xia, Q. & Fan, Q. 2011. Effect of water on the electrical  
828 conductivity of lower crustal clinopyroxene. *Journal of Geophysical Research: Solid Earth* **116**(B4).
- 829 81. Ye, G., Unsworth, M., Wei, W., Jin, S. & Liu, Z. 2019. The Lithospheric Structure of the Solonker  
830 Suture Zone and Adjacent Areas: Crustal Anisotropy Revealed by a High-Resolution Magnetotelluric  
831 Study. *JGR Solid Earth* **124**(2), 1142-1163.
- 832 82. Yoshino, T., Shimojuku, A., Shan, S., Guo, X., Yamazaki, D., Ito, E., ... & Funakoshi, K. I. 2012. Effect  
833 of temperature, pressure and iron content on the electrical conductivity of olivine and its high-  
834 pressure polymorphs. *JGR Solid Earth* **117**(B8).
- 835 83. Zhang, B. & Yoshino, T. 2017. Effect of graphite on the electrical conductivity of the lithospheric  
836 mantle. *Geochemistry, Geophysics, Geosystems* **18**(1), 23-40.
- 837 84. Zhu, W., Gaetani, G. A., Fusses, F., Montési, L. G. & De Carlo, F. 2011. Microtomography of partially  
838 molten rocks: three-dimensional melt distribution in mantle peridotite. *Science* **332**(6025), 88-91.